
# ENSO Precipitation Anomalies along the Equatorial Pacific: Moist Static Energy Framework Diagnostics

H. ANNAMALAI

*International Pacific Research Center/Department of Oceanography, University of Hawai'i at Mānoa, Honolulu, Hawaii*

(Manuscript received 22 May 2019, in final form 21 May 2020)

ABSTRACT

With the recognition that equatorial Pacific precipitation anomalies are fundamental to global teleconnections during ENSO winters, the present research applies vertically integrated moist static energy (MSE) budget analysis to historical simulations of CMIP5 models. Process-based assessment is carried out to understand if the models capture the differing processes that account for regional precipitation anomalies along the equatorial Pacific and to isolate a few leading processes that account for the diversified precipitation response to similar SST forcing and vice versa. To assess SST biases in CMIP5, analysis is also carried out in AMIP5 solutions. Diagnostics reveal that models have limitations in representing the ''sign'' of MSE sources and sinks and, even if they do, compensating errors dominate the budget. The diverse response in precipitation depends on model parameterizations that determine anomalous net radiative flux divergence in the column, free troposphere moisture, and MSE export out of the column, although these processes are not independent. Diagnostics derived from AMIP5 solutions support the findings from CMIP5. The implication is that biases in representing any one of these processes are expected to imprint on others, acknowledging the tight connections among moisture, convection, and radiation. CMIP5 models have limitations in representing the basic states in SST and precipitation over the Niño-3.4 region, and the different convective regimes over the equatorial central and eastern Pacific regions with implications for ENSO. Study limitations are that MSE sources/sinks depend on parameterizations and their interactions, making it difficult to isolate one particular process for attribution. Budgets estimated from monthly anomalies do not capture contributions from high-frequency variability that are vital in closing the budgets.

KEYWORDS: ENSO; Diagnostics; Model evaluation/performance

## 1. Introduction

### a. Background

Sustained research in observations, theory, and numerical modeling has demonstrated that sea surface temperature (SST) anomalies associated with El Niño–Southern Oscillation (ENSO) serve as an important source of predictability of seasonal to interannual climate anomalies over North America and the U.S.-affiliated Pacific islands (USAPI). Ignoring many complexities, the conceptual framework of how El Niño influences seasonal atmospheric anomalies over these regions can be summarized as follows: in response to positive SST anomalies along the equatorial central and eastern Pacific, surface fluxes and column moist static energy (MSE) increase locally, favoring convection and in the release of latent heating; subsequently, the upper-level divergence forces planetary Rossby waves that project onto the Pacific–North American pattern (Hoskins and Karoly 1981; Horel and Wallace 1981). Over the tropical latitudes, meridional displacement of the South Pacific convergence zone (SPCZ; Widlansky et al. 2011) toward warmer equatorial SST anomalies associated with El Niño and attendant modulations to the planetary Walker and local Hadley circulations exert considerable control on the seasonal rainfall anomalies over the USAPI (Annamalai et al. 2014). Recognizing that the equatorial Pacific precipitation and the associated diabatic heating anomalies are fundamental to this conceptual framework, the present research applies a suite of process-oriented diagnostics (POD; Maloney et al. 2019) relevant to moist convection, and identifies leading processes that translate ENSO-related SST anomalies into precipitation anomalies along

*Corresponding author*: H. Annamalai, hanna@hawaii.edu

DOI: 10.1175/JCLI-D-19-0374.1

the equatorial Pacific. With a focus on El Niño and La Niña winters, the POD is applied to historical simulations of available models in the CMIP5 database (phase 5 of the Coupled Models Intercomparison Project; Taylor et al. 2012) and reanalysis products.

In evaluating ENSO in CMIP3 and CMIP5 models, Bellenger et al. (2014) note that precipitation anomalies along the equatorial central Pacific are still poorly represented in CMIP5. Kug et al. (2012) conclude that successful simulation of spatial distribution of precipitation is a prerequisite for realistic representation of the full range of ENSO behavior in climate models (see also Capotondi et al. 2015). Despite dedicated efforts by the modeling community, progress in reducing the tropical precipitation biases is rather slow. A complementary approach is to apply the POD to identify aspects of parameterizations that may have limitations across models, and to suggest pathways for improvements.

Focusing on the 1997/98 El Niño, Su and Neelin (2002) applied moisture and MSE budget analyses to solutions obtained from the quasi-equilibrium tropical circulation model (QTCM). They noted that over the main El Niño warm SST anomaly region, enhanced latent heat flux anomalies are the leading process to promote positive precipitation anomalies. Annamalai et al. (2014) applied MSE budget analysis to the ensemble hindcasts performed with the Climate Forecast System, version 2 (CFSv2), and the ECMWF interim reanalysis (ERA-Interim). Recognizing that during boreal winter climatologically MSE is exported (imported) over the equatorial western (eastern) Pacific (Back and Bretherton 2006) in association to different convective regimes (Yuan and Hartmann 2008), and that ENSO-related precipitation anomalies occur basinwide (Fig. 2a), Annamalai et al. (2014) performed diagnostics separately for the equatorial central and eastern Pacific regions. Their major findings include that during El Niño winters, positive precipitation anomalies along the central equatorial Pacific are accounted for by horizontal moist advection and net radiative flux divergence in the column ($F_{\text{rad}}$). A further decomposition of the moisture advection equation indicates the importance of anomalous near-surface westerlies in advecting the climatological moisture gradient that prevails between the equatorial western and central Pacific (see Fig. 7d). In contrast, positive precipitation anomalies along the eastern equatorial Pacific are anchored by surface evaporation. Here, we will examine if CMIP5 models represent these differences in the processes that determine regional precipitation anomalies along the equatorial Pacific.

Many studies have highlighted that the treatment of moist convection in climate models is undoubtedly the single most problem for simulated precipitation biases in the tropics (e.g., Slingo et al. 1996). Based on radiosonde observations, Numaguti et al. (1995) and Ushiyama et al. (1995) suggest that a relatively moist low to midtroposphere initiate deep convection, and cloud-resolving models suggest that deep convection is sensitive to tropospheric humidity (Grabowski 2003; Derbyshire et al. 2004; Kuang and Bretherton 2006; Tulich and Mapes 2010), a result confirmed in numerical models (Woolnough et al. 2010) and in satellite observations (Bretherton et al. 2004). Diagnosing hourly observations, Holloway and Neelin (2009) show that precipitation intensity is highly correlated not with boundary layer humidity ($\text{BL}_q$) but rather with moisture in the free troposphere ($\text{FT}_q$). While $\text{BL}_q$ is determined by surface fluxes and cold pools associated with downdraft (Raymond 1995) $\text{FT}_q$ is determined by moisture–convection feedbacks (Bretherton et al. 2006) that are constrained by convection itself (Bretherton et al. 2006; Neelin et al. 2009).

Another factor that influences moist convection is cloud–radiation feedbacks (e.g., Yuan and Hartmann 2008). The interpretation is that anvil clouds from deep convection are effective in trapping longwave radiation causing a reduction in radiative cooling that subsequently feedbacks to convection through changes to column diabatic heating and omega profiles (Wolding et al. 2016). Note that $F_{\text{rad}}$ reacts to convection (Stephens et al. 2008) as well as contributing to convection (Wolding et al. 2016). Therefore, for realistic simulation of ENSO-related precipitation anomalies along the equatorial Pacific, model parameterizations need to adequately represent processes that are inherently tied to convection.

### b. *Present study*

Figure 1 shows CMIP5 models' fidelity in translating SST anomalies into precipitation anomalies over the Niño-3.4 region during El Niño (Fig. 1a) and La Niña (Fig. 1b) winters. Unless otherwise stated, results presented here are composites based on years when Niño-3.4 (5°S–5°N, 120°–170°W) SST anomalies exceed ±1.0 standard deviation. In the models, SST standard deviations range from 0.6° to 1.8°C. The following inferences are made from Figs. 1a and 1b: 1) simulated SST and precipitation are associated but that association is not perfect; 2) during El Niño winters, there are diverse responses in precipitation at SST values around 0.7°, 1.1°, 1.4°, 1.8°, 2.5° and 3.0°C; 3) diversity in precipitation responses is even more stronger during La Niña winters at SST values around −1.8°, −1.4°, and −1.0°C; and 4) in both winters, the precipitation response is similar to a range of SST anomalies (e.g., precipitation around 140 $\text{W m}^{-2}$ for SST ranging from 1.5° to 3.0°C during El Niño; Fig. 1a). Besides biases in SST, model parameterizations appear responsible for the diverse precipitation response. We are

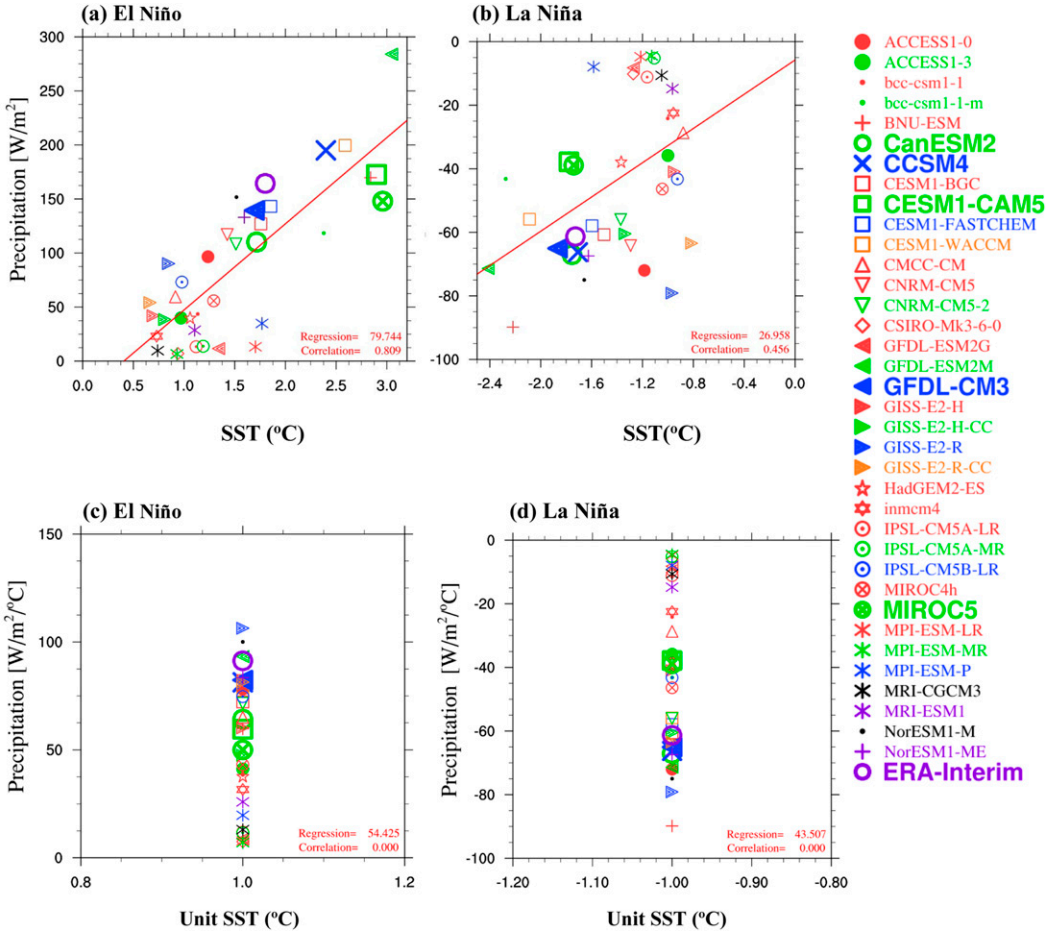


FIG. 1. Scatterplots between CMIP5 models simulated sea surface temperature (SST; °C) and precipitation ($W m^{-2}$). Shown are composite anomalies estimated for boreal winter (December–February) over the Niño-3.4 region (5°S–5°N, 120°–170°W): (a) El Niño and (b) La Niña. (c),(d) As in (a) and (b), but scaled by individual model simulated SST anomalies (unit SST). In all the panels, corresponding results from ERA-I are shown. Intermodel correlations between the two variables and the best-fit regression lines are also shown.

interested in understanding if model processes and their interactions relevant to moist convection account for these diverse responses. Details on how to interpret the scatterplots with relevance to the focus are given in section 2d.

Figure 2a shows observed precipitation anomalies and total SST ($SST_{cli} + SST_{anom}$) during El Niño winters; the suggestion is that concentrated positive precipitation anomalies are observed around the date line where total SST exceeds 28°C. In models, spreads in precipitation response to SST around 28°–29°C during El Niño (Fig. 2b), and around 24°–25°C during La Niña (Fig. 2c) are particularly striking. The decreasing precipitation anomalies to increasing total SST during La Niña (Fig. 2c) are due to the plotting convention. Note that models with strong El Niño (CESM1-CAM5 and MIROC5) do not capture a wet bias (Fig. 1a), possibly due to a weak climatology (details in section 5). A question of interest is this: to what degree does the simulation of basic states in SST and precipitation impact ENSO-related precipitation anomalies?

Figure 1a suggests that compared to observations, most models simulate weaker SST and attendant precipitation anomalies and such biases clearly inflate the linkages. To assess this, each model's simulated precipitation and SST anomalies are scaled by the respective SST anomalies (i.e., precipitation response to unit SST) and the results are shown for El Niño (Fig. 1c) and La Niña (Fig. 1d). In both winters, scaling also highlights models' diverse response (or spread) in precipitation ranging from near zero to $\pm 100\,W m^{-2}$. Note that the scaling comes with a caveat: in the deep tropics, the relationship between SST and precipitation [or SST and column water vapor (CWV) or column relative humidity (CRH)] is highly nonlinear (e.g., Graham and Barnett 1987; Neelin et al. 2009) and also asymmetric (warm vs cold SST anomalies; Figs. 2b,c). The nonlinearity is

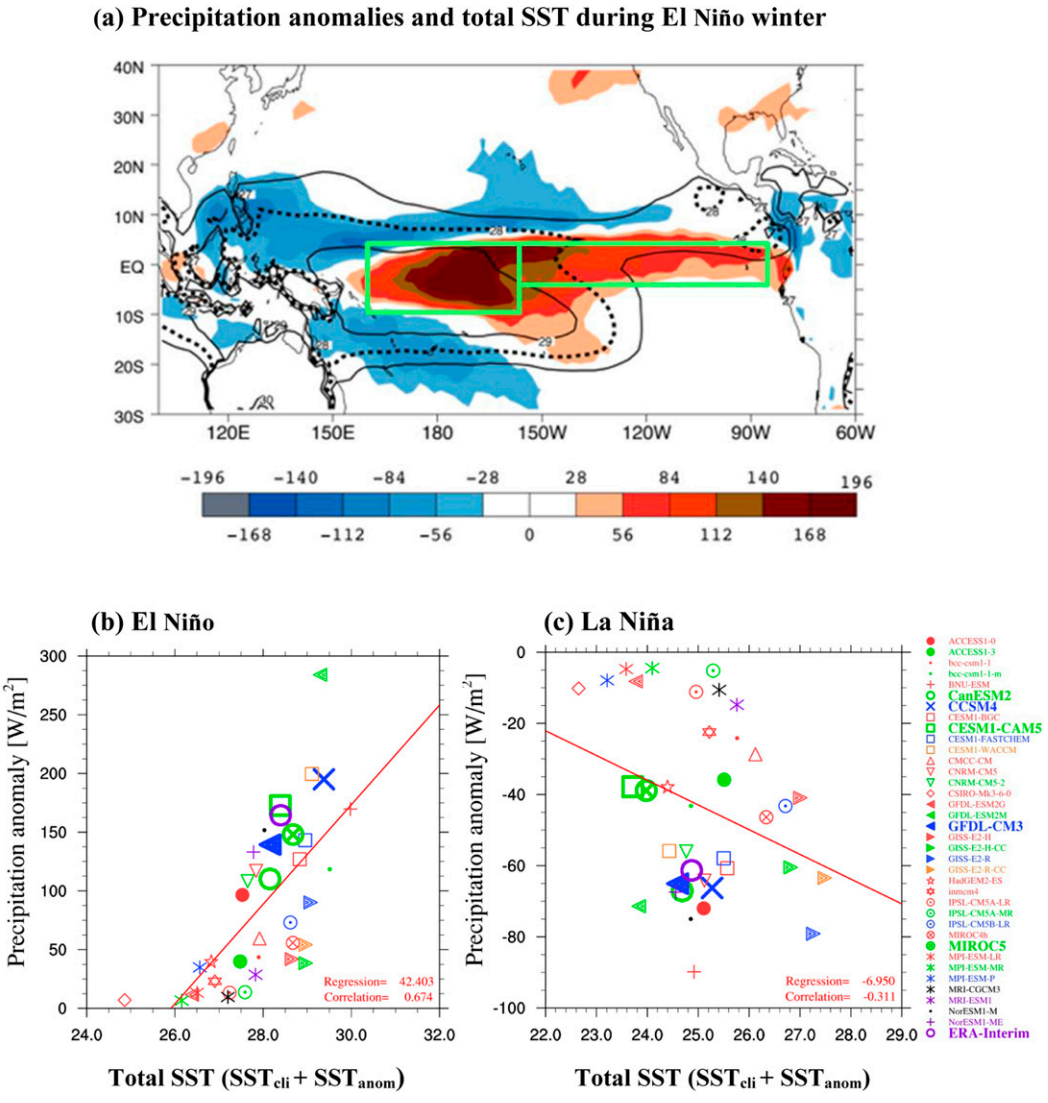


FIG. 2. (a) Observed composite precipitation anomalies (shaded; W m$^{-2}$) and total SST (contours; 28°C isotherm is dotted) during El Niño winter. (b),(c) Scatterplots between CMIP5 models simulated total SST (°C) and anomalous precipitation (W m$^{-2}$), showing composites estimated for boreal winter (December–February) over the Niño-3.4 region (5°S–5°N, 120°–170°W) for El Niño and La Niña, respectively. Total SST is the model's simulated SST climatology plus SST anomalies. In (a), boxed regions show the equatorial central Pacific (10°S–5°N, 160°E–160°W) and eastern Pacific (5°S–5°N, 160°–80°W), used to average the various diagnostics presented here.

clearly evident in the SST range of 27.5°–29.5°C (e.g., Neelin et al. 2009), regions where maximum ENSO-related precipitation anomalies are observed (Fig. 2a) while the models' response varies from near zero to 200 W m$^{-2}$ (Fig. 2b). Another normalization based on each model's SST standard deviation also does not account for the nonlinearity (figure not shown). An alternative approach is to diagnose AMIP5 simulations in which observed SST is used to force the atmospheric component of the coupled models, and we follow that approach here. Further discussion on how to interpret the scatterplots is given in section 2d.

Within the realism of limited observations over the tropical oceans, understanding and quantifying processes (dynamics and thermodynamics, and their inherent nonlinear feedbacks) that determine precipitation is challenging. In the deep tropics, due to the smallness of the Coriolis force and large Rossby radius of deformation, stratified adjustment by internal gravity waves is able to rapidly eliminate horizontal temperature gradients, particularly above the planetary boundary layer, and in this weak temperature gradient (WTG) approximation (Charney 1963; Sobel et al. 2001; Bretherton and Sobel 2003) tropical precipitation is linked to vertically integrated MSE or

equivalently to moisture anomalies (Neelin and Held 1987; Bretherton et al. 2006). We hypothesize that models' fidelity in representing ENSO-related precipitation anomalies requires their ability in representing processes that determine column MSE anomalies.

We are interested in seeking answers to questions such as the following: Do models capture the differing processes that account for regional precipitation anomalies along the equatorial Pacific? Are there few leading processes that account for diversified precipitation response to similar SST forcing and vice versa? To test the hypothesis and address related questions first we assess precipitation versus moisture variations over the column, boundary layer, and free troposphere. Second, encouraged by the results, we apply vertically integrated MSE budget to CMIP5 solutions and reanalysis products, and identify leading model processes that account for diversified precipitation responses. Third, we interpret interlinkages among the identified processes that acknowledge the tight connection among moisture, convection, and radiation. Finally, to assess the role of SST biases with regard to precipitation anomalies in CMIP5, diagnostics are repeated with AMIP5 solutions. Our POD show that diverse precipitation response depends on model parameterizations that determine $F_{rad}$, $FT_q$, and vertical advection of MSE.

The remainder of this article includes a brief description of the CMIP5 models, observations, and reanalysis products diagnosed along with budget equations (section 2), followed by discussions on basic POD along the equatorial Pacific (section 3), MSE budget diagnostics and construction of relevant metrics (section 4), inferences on improvements for climate models (section 5), and a summary and conclusions (section 6).

## 2. Data, models, and methods

### a. Observation and reanalysis products

Observational data include the merged satellite-derived precipitation product from the Tropical Rainfall Measuring Mission (TRMM) combined "TRMM and Other Satellite Precipitation Product" (3B42; Huffman et al. 2007), surface heat and evaporative fluxes from OAFlux (Yu et al. 2008), and Clouds and the Earth's Radiant Energy System (CERES) radiation data of Wielicki et al. (1996). To assess observational uncertainty, multiple observed SST products from the Hadley Centre's Sea Ice and Sea Surface Temperature dataset (HadISST; Rayner et al. 2003), the NOAA Extended Reconstructed SST (ERSST) version 4 (Huang et al. 2015), and the TRMM Microwave Imager (TMI; Wentz et al. 2000), as well as additional precipitation from the Global Precipitation Climatology Project (GPCP; Huffman et al. 2009), are used.

The bulk of atmospheric data used are taken from ERA-Interim (hereinafter ERA-I) products generated at the European Center for Medium-Range Weather Forecasts. ERA-I represents well the vertical distribution of moisture and thermodynamic variables, tropical precipitation, and its intraseasonal variability (Dee et al. 2011); therefore, it has been widely used for model validation (e.g., Hannah and Maloney 2014; Mohan et al. 2018). For the budget analyses, primary monthly variables diagnosed here include three-dimensional temperature ($T$), specific humidity ($q$), geopotential height ($z$), vertical pressure velocity ($\omega$), and zonal and meridional wind ($u$ and $v$) components. Surface variables such as precipitation and sensible (SH) and latent (LH) fluxes are also diagnosed. Additionally, net column longwave (LW) and shortwave (SW) radiation components are also analyzed.

To assess observational uncertainty, identification of El Niño and La Niña years was done both in HadISST and ERSST, and composites of relevant variables such as SST and precipitation (from TRMM and GPCP) are compared with those from ERA-I and other reanalysis products such as MERRA (Rienecker et al. 2011), JRA-25 (Onogi et al. 2007), and CFSR (Saha et al. 2010). Without going into details that are deferred for a future study, results from different SST and precipitation products are comparable both in spatial pattern and amplitude while ERA-I results are in good agreement with these observed composites. We recognize that in data-sparse regions such as the tropics, global analysis injects model prejudices (Raymond et al. 2009), and therefore ERA-I has its limitations as well.

### b. CMIP5/AMIP5 model simulations

Some features of CMIP5 models such as acronyms, symbols, and basic properties are listed alphabetically in Table 1. The suite consists of solutions from 36 models that have been examined earlier; see Sperber et al. (2013) and Nagura et al. (2018) for more details. Here, models' historical runs for the period 1951–2005 are diagnosed, that is, from their solutions forced by observed atmospheric composition changes and solar radiation. Model ENSO winters are identified as in observations, and diagnostics are applied to composite values. In the CMIP5 database, a suite of 22 atmosphere-only solutions forced with observed SSTs for the period 1979–2010 is also available. These solutions termed AMIP5 are also diagnosed.

### c. POD based on vertically integrated MSE budget

We developed the POD package based on vertically integrated MSE budget. Briefly, the vertically integrated MSE tendency is approximately given by

$$\left\langle \frac{\partial m}{\partial t} \right\rangle = -\langle \overline{\mathbf{V}} \cdot \nabla m \rangle - \left\langle \omega \frac{\partial m}{\partial p} \right\rangle + \mathrm{LH} + \mathrm{SH} + \langle \mathrm{LW} \rangle + \langle \mathrm{SW} \rangle, \quad (1)$$

TABLE 1. CMIP5 models, and horizontal and vertical resolutions of atmospheric and oceanic models.

| Model designation | AGCM horizontal and vertical resolution | OGCM horizontal and vertical resolution |
|---|---|---|
| ACCESS1.0 | 1.875° lon × 1.25° lat, L38 | 1° lon × 1° lat, L50 |
| ACCESS1.3 | 1.875° lon × 1.25° lat, L38 | 1° lon × 1° lat, L50 |
| BCC-CSM1.1 | T42, L26 | 1° lon × 1° lat, L40 |
| BCC-CSM1.1-m | 1.125° lon × 1.125° lat, L26 | 1° lon × 1° lat, L40 |
| BNU-ESM | T42, L26 | 1° lon × 1° lat, L50 |
| CanESM2 | T63, L31 | 256 × 192, L40 |
| CCSM4 | 1.25° lon × 0.9° lat, L26 | 1.1° lon × 0.27°–0.54° lat, L60 |
| CESM1-BGC | 1.25° lon × 0.9° lat, L17 | 1.25°lon × 0.9° lat, L60 |
| CESM1-CAM5 | 1.25° lon × 0.9° lat, L17 | 1.25°lon × 0.9° lat, L60 |
| CESM1-FASTCHEM | 1.25° lon × 0.9° lat, L17 | 1.25°lon × 0.9° lat, L60 |
| CESM1-WACCM | 2.5° lon × 1.9° lat, L23 | 2.5°lon × 1.9°, L60 |
| CMCC-CM | 0.75° lon × 0.75° lat, L17 | ~2° lon × ~2° lat, L31 |
| CNRM-CM5 | T127, L31 | 1° lon × 1° lat, L42 |
| CNRM-CM5.2 | T63, L18 | 1.875° lon × ~0.9375° lat, L31 |
| CSIRO-Mk3.6.0 | T63, L18 | 1.875° lon × 0.925° lat, L31 |
| GFDL-ESM2G | M45, L24 | 360 × 200, L63 |
| GFDL-ESM2M | M45, L24 | 360 × 200, L50 |
| GFDL CM3 | C48, L48 | 360 × 200, L50 |
| GISS-E2-H | 2.5° lon × 2° lat, L40 | 2.5° lon × 2° lat, L40 |
| GISS-E2-H-CC | 2.5° lon × 2° lat, L40 | 2.5° lon × 2° lat, L40 |
| GISS-E2-R | 2.5° lon × 2° lat, L40 | 1° lon × ~1° lat, L32 |
| GISS-E2-R-CC | N96, L60 | 1° lon × ~0.3°–1.0° lat, L40 |
| HadGEM2-ES | N96, L38 | 1° lon × ~0.3°–1.0° lat, L40 |
| INM-CM4 | 2° lon × 1.5° lat, L21 | 1° lon × 0.5° lat, L40 |
| IPSL-CM5A-LR | 96 × 95, L39 | 2° lon × 2° lat, L31 |
| IPSL-CM5A-MR | 144 × 143, L39 | 2° lon × 2° lat, L31 |
| IPSL-CM5B-LR | 3.75° × 2°, L39 | 2° lon × 2° lat, L31 |
| MIROC4h | T213, L56 | 1280 × 912, L48 |
| MIROC5 | T85, L40 | 256 × 224, L50 |
| MPI-ESM-LR | T63, L47 | GR15, L40 |
| MPI-ESM-MR | T63/1.9°, L95 | TP04, L40 |
| MPI-ESM-P | T63/1.9°, L47 | GR15, L40 |
| MRI-CGCM3 | TL159, L48 | 1° lon × 0.5° lat, L51 |
| MRI-ESM1 | TL159, L23 | 1° lon × 0.5° lat, L51 |
| NorESM1-M | 144 × 96, L26 | 384 × 320, L53 |
| NorESM1-ME | 2.5° lon × 1.9° lat, L17 | 1.1° lon × 0.6° lat, L70 |

where $m$ is MSE, $\mathbf{V}$ is the horizontal velocity vector, $\langle \mathrm{LW} \rangle$ and $\langle \mathrm{SW} \rangle$ are net column integrated longwave and shortwave heating rates, $\omega$ is vertical pressure velocity, LH and SH are surface fluxes of latent and sensible heat, and $p$ is pressure. The angle brackets $\langle\rangle$ represent vertical integrals, and in the present study integration is done between the 1000- and 100-hPa levels; $F_{\mathrm{rad}}$ is the sum of $\langle \mathrm{LW} \rangle$ and $\langle \mathrm{SW} \rangle$. At seasonal time scales considered here, the storage term is neglected. Regarding diabatic terms, model surface parameterization schemes estimate LH and SH fluxes while $\langle \mathrm{LW} \rangle$ and $\langle \mathrm{SW} \rangle$ calculations depend on longwave and shortwave parameterizations. The adiabatic terms $\langle -\mathbf{V} \cdot \nabla m \rangle$ and $\langle -\omega m_p \rangle$ partly depend on the dynamical cores, and partly on the horizontal and vertical ($m_p$) MSE gradients. Furthermore, the $\omega$ profile in the deep tropics is tightly associated to diabatic heating profile (Hartmann et al. 2001; Back et al. 2017) that is determined by cloud–convection–radiation interactions (Bony et al. 2004). In summary, all MSE terms depend on model parameterizations and their interactions, and therefore, it is difficult to isolate one particular model process for attribution when examining climate equilibrium solutions.

### d. Metrics

Following our earlier work (Nagura et al. 2018), results are presented in a series of scatterplots between pairs of model variables deemed "physically consistent," meaning that the two variables are physically linked but not that one variable is determining the other (i.e., the plots do not reveal any causality). Briefly, scatterplots are obtained between two variables; to assess if the two variables are linked, a measure of the goodness of fit is the correlation coefficient $C$, and for the total models considered here, $C$ values $> 0.28$ pass the 95% confidence level. In each scatterplot, we also plot lines that best fit all of the data points; our interest lies in models that are away from the best fit line.

Keeping these statistics as guidance, physical interpretations are discussed, and leading processes contributing to

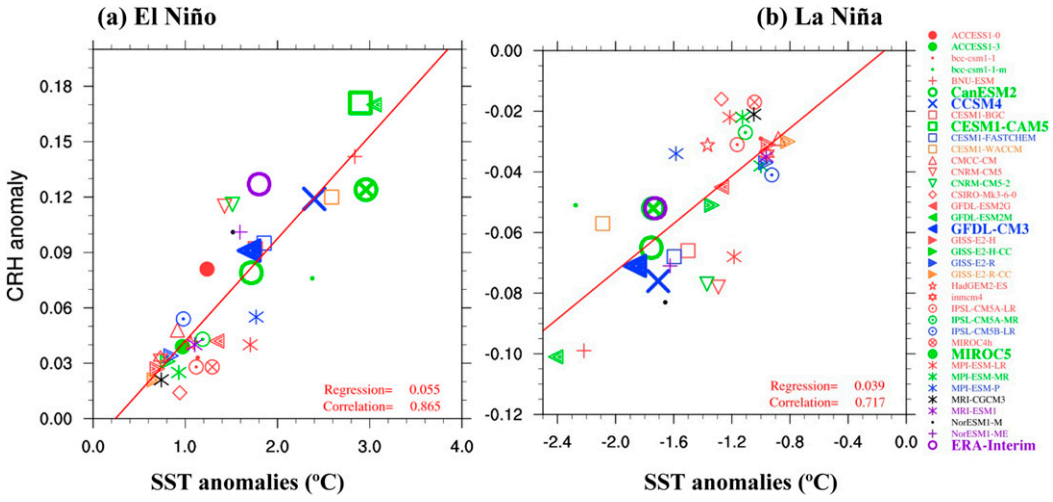


FIG. 3. Scatterplots between CMIP5 models simulated sea surface temperature (SST; °C) and column relative humidity (CRH). Shown are composite anomalies estimated for boreal winter (December–February) over the Niño-3.4 region (5°S–5°N, 120°–170°W): (a) El Niño and (b) La Niña. Corresponding results from ERA-I are shown. Intermodel correlations between the two variables and the best-fit regression lines are also shown.

systematic errors in the simulated precipitation anomalies are identified. Systematic errors in climate models are defined as "the departure of the simulated climate statistics from the observed" (e.g., by a difference in monthly means; Phillips et al. 2004, p. 1903). High values of intermodel correlation suggest the existence of a linear relationship that in our case is partly influenced by SST biases. However, these results do not change if scaling is performed either by individual model SST anomalies (unit SST as shown in Figs. 1c and 1d) or by individual model standard deviation of SST (not shown). In such scaling care should be taken into account because of the inherent nonlinear relationship between SST and precipitation as well as asymmetric precipitation response to warm versus cold SST anomalies (Figs. 2b,c). Furthermore, realistic simulation of precipitation anomalies during El Niño (La Niña) may depend on models' ability in correctly simulating SST (precipitation) climatology (section 5). Finally, showing actual simulated values benefits the modeling community to assess the contribution of individual MSE terms to precipitation, and thereby recognize compensating errors. In the discussions to follow, efforts are made to understand the diverse response (i.e., deviations from the regression lines) and identify leading processes for such diversity. Extra care is devoted not to discuss results influenced by SST biases leading to erroneous simulation in model processes (e.g., moisture and MSE terms).

## 3. Basic diagnostics

In this section, we begin by discussing results between SST and CRH anomalies (section 3a), followed by precipitation versus moisture variations over 1) the column, 2) the boundary layer, and 3) the free troposphere (section 3b). These results pave ways to justify MSE budget diagnostics employed in section 4.

### *a. SST anomalies versus CRH anomalies*

Satellite observations over the tropical oceans suggest a strong relationship between SST and CWV or CRH (Raymond 2000; Bretherton et al. 2004; Neelin et al. 2009; Kanemaru and Masunaga 2013), a relationship that holds during ENSO over the tropical Pacific (Trenberth et al. 2005). A plausible interpretation is that SST anomalies induce surface fluxes leading to increased boundary layer moisture anomalies ($BL_q'$), which allows conditional instability to be realized and convection to develop. By detrainment processes, shallow convection gradually moistens the free troposphere. In a circular argument, CRH acts as a "bridge" between SST and precipitation. In both winters (Fig. 3), while diversities in CRH at various SST values are prevalent compared to such diversities in precipitation at the same SST values (Figs. 1a,b), the spread among the models is relatively less in Fig. 3. However, efficiency in translating CRH into precipitation varies among models. During El Niño (Fig. 3a), models that simulate a range of SST anomalies (1.6°–3.0°C) capture CRH anomalies (~0.12) that are close to ERA-I but their precipitation response varies from one model to other (Fig. 1a). For comparable SST and CRH anomalies, precipitation diversity is particularly strong between CESM1-CAM5 (~160 $W m^{-2}$) and GFDL-ESM2M (~280 $W m^{-2}$), possibly due to different basic states (section 5b). Models that capture realistic (or observed) SST anomalies simulate diverse

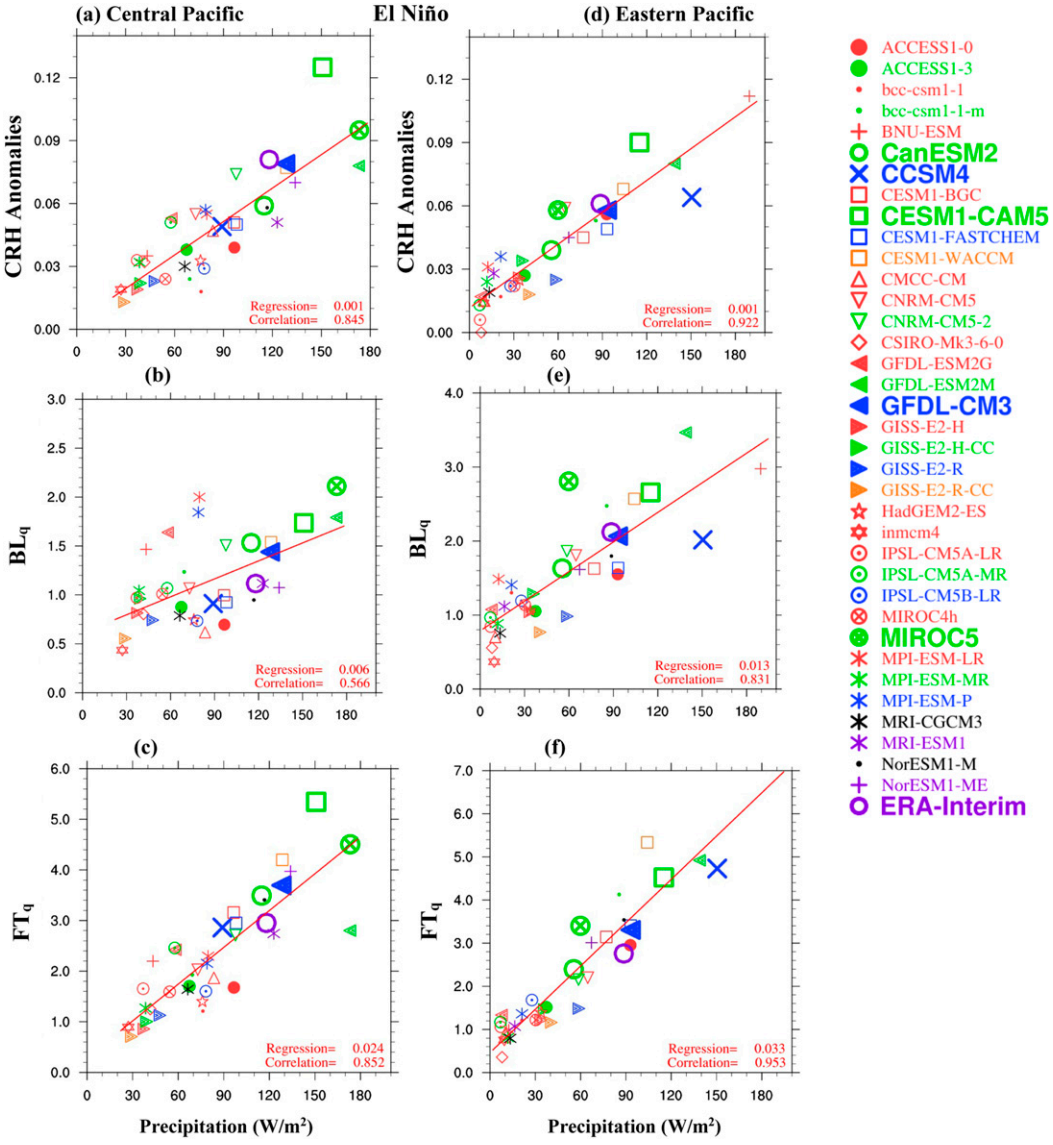


FIG. 4. Scatterplots between CMIP5 models' simulated precipitation ($W\,m^{-2}$) and (a),(d) column relative and specific humidity in (b),(e) the boundary layer and (c),(f) the free troposphere. Shown are composite anomalies during El Niño winters, and averaged over the equatorial (left) central and (right) eastern Pacific. Intermodel correlations and best-fit regression lines are also shown.

CRH anomalies (~0.05–0.12) with similar imprints in precipitation (note the alignment above and below the regression line in Fig. 1a compared with Fig. 3a). During La Niña too (Fig. 3b), diversities in CRH to SST anomalies (−1.8°, −1.2°, and −0.8°C) and corresponding precipitation diversities (Fig. 1b) are noted. During both ENSO winters, observed maxima in precipitation anomalies occur over the equatorial central Pacific where total SST exceeds 28°–29°C (Fig. 2a) with sharp increases in CRH (Kanemaru and Masunaga 2013). One plausible interpretation is that the large spread in CRH anomalies around observed SST values (Figs. 3a,b) may possibly be related to models' inability to capture sharp changes in CRH with implications in precipitation spread around SST values ~28°–29°C (Fig. 2b).

### b. *Anomalous precipitation versus vertical moisture distribution*

For El Niño winters, Fig. 4 shows scatterplots between anomalous precipitation and CRH (top), $BL'_q$ (middle), and $FT'_q$ (bottom) moisture variations, separately for the

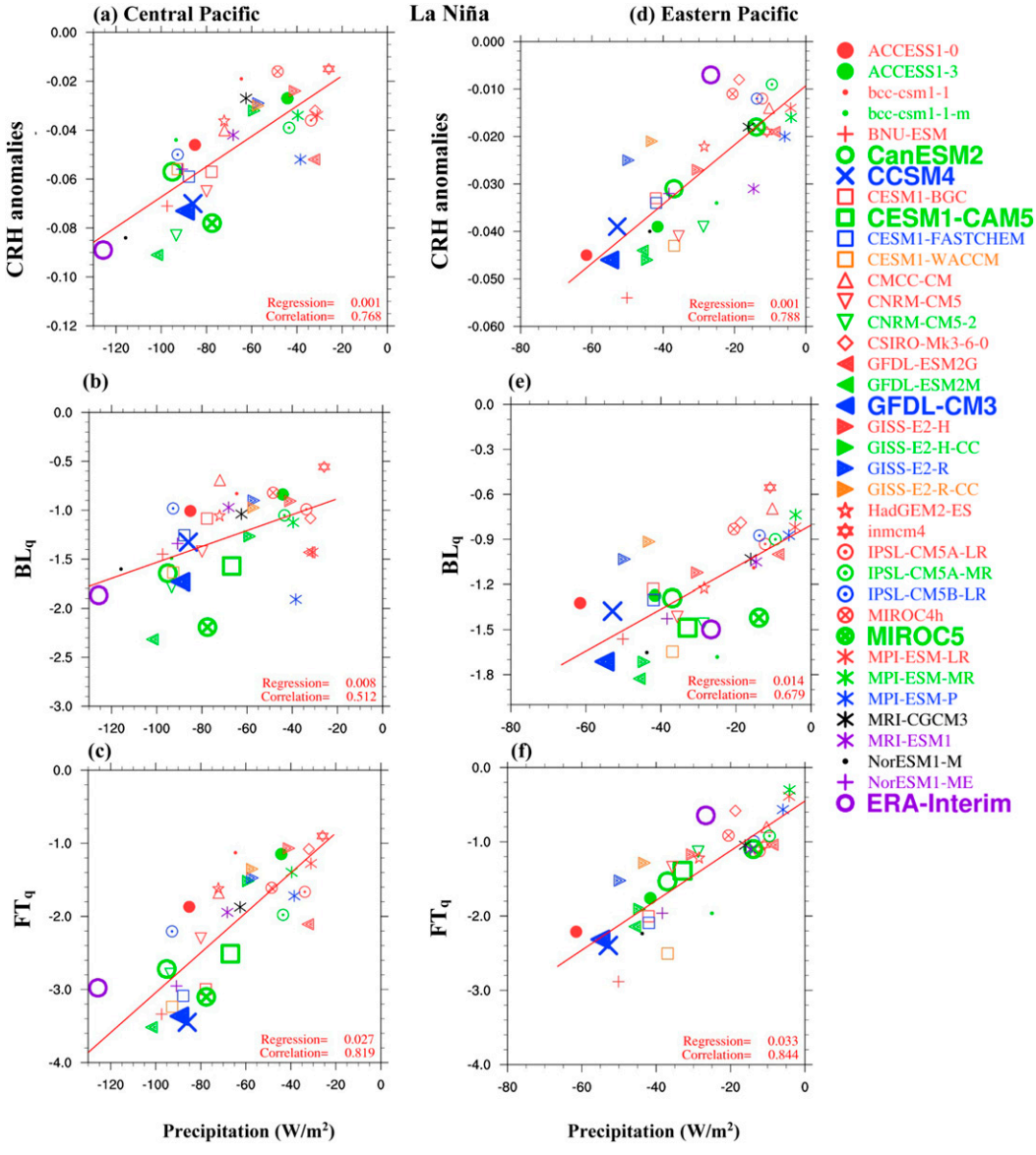


FIG. 5. As in Fig. 4, but for La Niña winters.

central (left) and eastern (right) Pacific. Similar diagnostics for La Niña winters are shown in Fig. 5. During El Niño in both regions (Fig. 4), mainly due to SST biases, many models simulate weaker CRH/$FT_q'$ and less positive precipitation anomalies. Similarly during La Niña (Fig. 5), models simulate less dryness and weaker precipitation anomalies over the central Pacific. In contrast over the eastern Pacific, more dryness and stronger negative precipitation anomalies are simulated. During El Niño, ERA-I results suggest that $BL_q'$ and $FT_q'$ (Figs. 4b,c) are comparable over the eastern Pacific (~2.2 and 2.6) while their variations differ by nearly 3 times over the central Pacific (~1.0 and 2.8). Indeed many models represent the relative ratios between $BL_q'$ and $FT_q'$ in the two regions (Fig. 4b vs Fig. 4c; Fig. 4e vs Fig. 4f). During La Niña over the eastern Pacific, ERA-I results suggest that dryness over $BL_q'$ (Fig. 5e) is stronger than that over $FT_q'$ (Fig. 5f) but vice versa over the central Pacific (Figs. 5b,c), and models fail to represent these features correctly (Figs. 5a,d). During El Niño over the central Pacific, large diversities in $BL_q'$ and $FT_q'$ are evident around precipitation values of ~60–120 W $m^{-2}$ (Figs. 4b,c), and similar diversities over the eastern Pacific are noticeable around precipitation values of ~60–100 W $m^{-2}$ (Figs. 4e,f). One interpretation is that $BL_q'$ is determined by surface fluxes and cold pools associated with downdraft (Raymond 1995). In models, the $BL_q'$ diversity may reflect insufficient representation of cold pools. Similarly, diversities in $FT_q'$

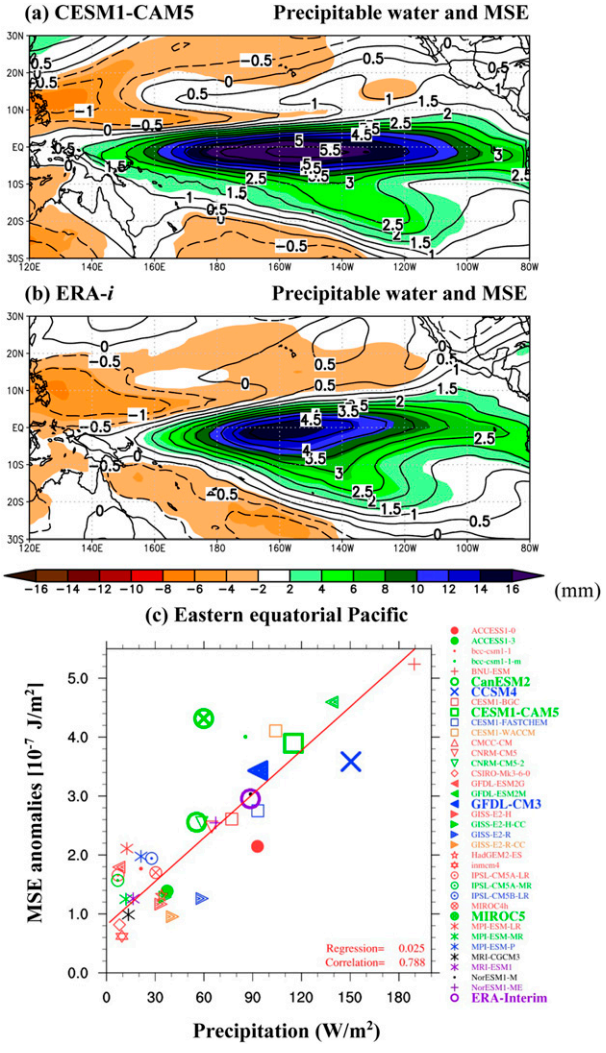


FIG. 6. Vertically integrated anomalous moist static energy (MSE; contours; J m$^{-2}$) and precipitable water (PW; shaded; mm) for the composite El Niño winter season (December–February): (a) CESM1-CAM5 and (b) ERA-I, and (c) scatterplots between CMIP5 models simulated vertically integrated MSE anomalies and precipitation anomalies estimated for boreal winter composites over the eastern equatorial Pacific (5°S–5°N, 160°–80°W). MSE values are scaled by $10^{-7}$, and in (a) and (b) negative contours are dotted. In (c) intermodel correlations between the two variables and the best-fit regression lines are also shown.

may be attributed to representation of moisture–convection feedbacks (see more discussion in sections 4 and 5). In summary, a relevant finding is that, during both El Niño and La Niña winters, model diversity in CRH/FT$'_q$ is strongly imprinted in precipitation spread. The sensitivity of CRH/FT$'_q$ to precipitation motivates identifying processes that determine column MSE anomalies.

For composite El Niño winters, Fig. 6 shows vertically integrated anomalous MSE (contours) and specific humidity (shading) from the CESM1-CAM5 climate model (Fig. 6a) and ERA-I (Fig. 6b). Alternately, vertically integrated specific humidity is precipitable water (PW) or CWV. In regions of organized positive and negative PW anomalies along the equatorial Pacific, structure and intensity of MSE and PW anomalies bear a "close association," implying that column MSE anomalies determine PW anomalies (e.g., Bretherton et al. 2006; Zhao et al. 2018). Consistent with CRH/FT$'_q$, models' column MSE and precipitation anomalies averaged over the eastern equatorial Pacific during El Niño depict an association (Fig. 6c). Around precipitation values of ~60–90 W m$^{-2}$, models that deviate from the regression lines noted in CRH, BL$'_q$, and FT$'_q$ (Figs. 4d–f) broadly align in the column MSE anomalies too.

## 4. MSE budget diagnostics

Here, we show observed characteristics during El Niño winter to highlight processes that models need to represent from MSE budget analysis (section 4a), followed by discussions between MSE terms and precipitation (section 4b). For composite El Niño and La Niña winters, we applied Eq. (1). In a steady state, combined contributions from sources and sink should cancel out. It needs to be mentioned here that we applied budget diagnostics on monthly anomalies and therefore the analysis does not capture contributions from high-frequency synoptic systems and eddies that play key roles in closing the budgets, particularly over the eastern Pacific (Peters et al. 2008). Therefore, our results do have limitations.

### a. Observed characteristics

For El Niño winter, Fig. 7 shows observed composites of variables relevant to MSE budget analysis. Our interpretations are supported by diagnostics obtained from ERA-I (Figs. 8 and 9). As regards to diabatic terms: near-equatorial low-level wind anomalies oppose climatological easterlies along the equatorial central-eastern Pacific, and therefore positive surface total heat flux (THF) anomalies (Fig. 7c), primarily due to LH fluxes, develop as direct responses to warm SST anomalies (Fig. 7a) with subsequent increases in BL$'_q$ (e.g., Fig. 4e); observed precipitation anomalies (Fig. 2a) depict a local maximum over the equatorial central Pacific (160°E–160°W) where positive $F_{\mathrm{rad}}$ anomalies (Fig. 7b) show high values (~30–40 W m$^{-2}$) indicating the response of convection to $F_{\mathrm{rad}}$. Regarding adiabatic or advective terms: in response to precipitation-induced diabatic heating anomalies, east–west Walker and north–south local Hadley circulations are modulated with implications to $\langle -\mathbf{V}\cdot\nabla q\rangle'$. Specifically, low-level westerly anomalies advect climatological high PW or MSE air from the equatorial

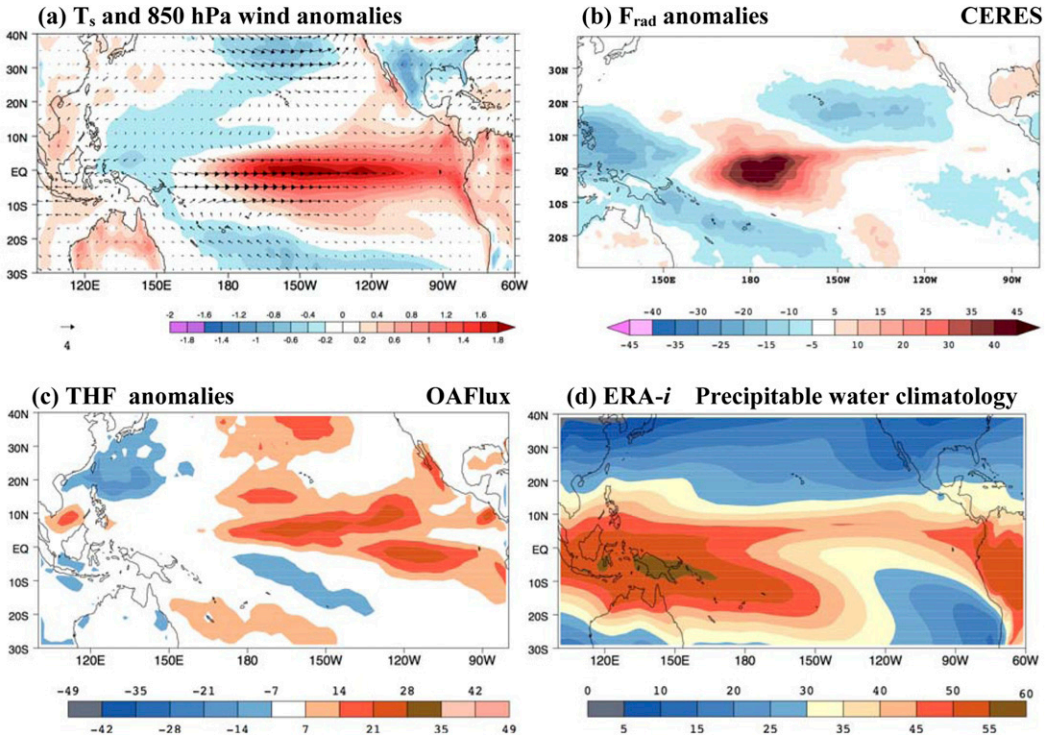


FIG. 7. Observed boreal winter (December–February) composite El Niño–related anomalies in (a) surface temperature $T_s$ (°C) and 850-hPa wind anomalies (m s$^{-1}$); (b) net radiative flux divergence in the column $F_{rad}$ (W m$^{-2}$) from CERES observations; (c) surface total heat flux (THF; W m$^{-2}$) from OAFlux data, and (d) precipitable water climatology for boreal winter season (mm) derived from ERA-I for boreal winter. Unit vector for (a) is also shown.

western to the central Pacific while northerly anomalies advect low PW air from subtropics (20°–30°N) to the near-equatorial Pacific (Figs. 7d and 8a); furthermore, the vertical structure of omega (Fig. 10) determines the vertical advection of MSE, $\langle -\omega m_p \rangle'$. Note that diabatic and adiabatic MSE terms are not independent but mutually influence one another. The observed conditions during La Niña winter are a mirror image to El Niño and hence not shown.

### b. MSE budget analysis in CMIP5 models

In the plots, MSE terms are binned against precipitation, and all variables are expressed in energy units (W m$^{-2}$). As mentioned in section 2d, quantitatively the scatterplots illustrate each model's ability in representing individual terms' contributions to precipitation as well as highlight model compensating errors. We assess if the models capture the different processes that account for precipitation over the central and eastern Pacific, and whether or not the analysis explains diversified precipitation responses to similar CRH values and vice versa. Since vertical advection of MSE depends on the vertical structure of omega, Fig. 10 shows anomalous $\omega$ profiles averaged over the central (left) and eastern (right) equatorial Pacific during El Niño winters. In data-sparse tropical regions, $\omega$ from reanalysis is not observed but is inferred from the data assimilation system, and therefore is influenced by model physics (Raymond et al. 2009). Hence, diagnostics performed with JRA-25 are also shown.

#### 1) EL NIÑO

During El Niño (Figs. 8 and 9), positive values in $-\langle \mathbf{V} \cdot \nabla q \rangle'$, $F_{rad}$, and THF correspond to moist advection, reduced radiative cooling, and evaporation from the ocean to the atmosphere, respectively. Negative values in $-\langle \omega m_p \rangle'$ represent MSE export by the divergent circulation. With the sign conventions, ERA-I suggests that over the central Pacific $-\langle \mathbf{V} \cdot \nabla q \rangle'$, $F_{rad}$, and THF are net sources while $-\omega m_p'$ is the only sink, but over the eastern Pacific both adiabatic (diabatic) terms are sinks (sources) of column MSE anomalies. In summary, as alluded to in section 1, processes that contribute to column MSE are different between the equatorial central and eastern Pacific.

##### (i) Equatorial central Pacific

Of the MSE sources, more than half of the models incorrectly capture the contributions from $-\langle \mathbf{V} \cdot \nabla q \rangle'$ and THF (Figs. 8a,d) with implications to dampen

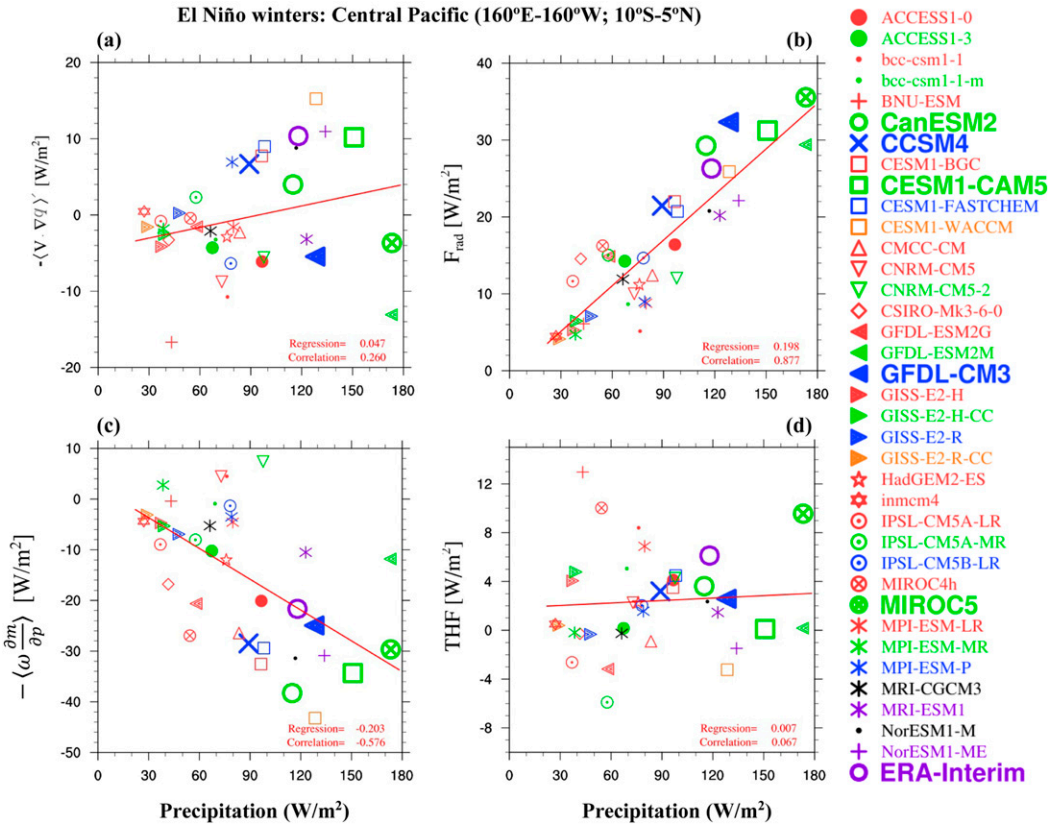


FIG. 8. Scatterplots between CMIP5 models simulated precipitation vs MSE budget terms: (a) horizontal advection of moisture, (b) net radiative flux divergence $F_{rad}$, (c) vertical advection of MSE, and (d) surface total heat flux (sensible + latent). Shown are budget terms estimated for El Niño winter composites and averaged over the equatorial central Pacific (10°S–5°N, 160°E–160°W). Results from ERA-I are also shown. In each panel, intermodel correlations and best-fit regressions are also provided.

column MSE and precipitation anomalies. ERA-I shows that contributions from $-\langle \mathbf{V} \cdot \nabla q \rangle'$ ($\sim$10 W m$^{-2}$) and THF ($\sim$5–6 W m$^{-2}$) are modest, implying a minimal role on precipitation anomalies. An investigation of the moisture advection equation suggests that models have limitations in representing the basic-state moisture gradient across the equatorial western and central Pacific (not shown), consistent with limitations in representing climatological features discussed later (section 5b). In ERA-I, the low contribution from THF is in agreement with modest observed SST anomalies ($\sim$0.6°C; not shown). Simulated SST anomalies lie in the range from 0.1° (CMCC-CM) to 1.6°C (MIROC5) with most around 0.5°–1.0°C (not shown). Yet, negative THF anomalies (primarily LHF) in many of the models warrant further investigations in assessing the relative roles of SST and surface wind speed on evaporation. On the other hand, $F_{rad}$ responds (and also feeds back) to positive precipitation anomalies and all the models get the sign correctly. Barring just a few models, the MSE sink term $-\langle \omega m \rangle'$ is faithfully represented and the intensity of MSE export is closely associated with the intensity and top-heavy characteristics of $\omega$ profiles (Fig. 10, left panels). Over the central Pacific, the dominant balance is between $F_{rad}$ and $-\langle \omega m_p \rangle'$, and the models that capture the signs of THF and $-\mathbf{V} \cdot \nabla q'$ correctly also represent the sources and sinks correctly. A closer examination, however, suggests compensating errors. For instance, $F_{rad}$ compensates for $-\langle \mathbf{V} \cdot \nabla q \rangle'$ in GFDL CM3 and MIROC5. Like in CRH results (Fig. 4a), for precipitation values around 90–120 W m$^{-2}$, large diversities in $F_{rad}$ and $-\langle \omega m_p \rangle'$ (Figs. 8b,c) are noticeable. Notable scattering in $F_{rad}$ (Fig. 8b) for similar precipitation ($\sim$120 W m$^{-2}$) or for similar $F_{rad}$ ($\sim$30 W m$^{-2}$) with a spread in precipitation (110–180 W m$^{-2}$) suggests constraints from model to model in adequately representing radiation anomalies. To summarize, models' parameterization schemes that determine $F_{rad}$ and $-\langle \omega m_p \rangle'$ account for the diversity in CRH and

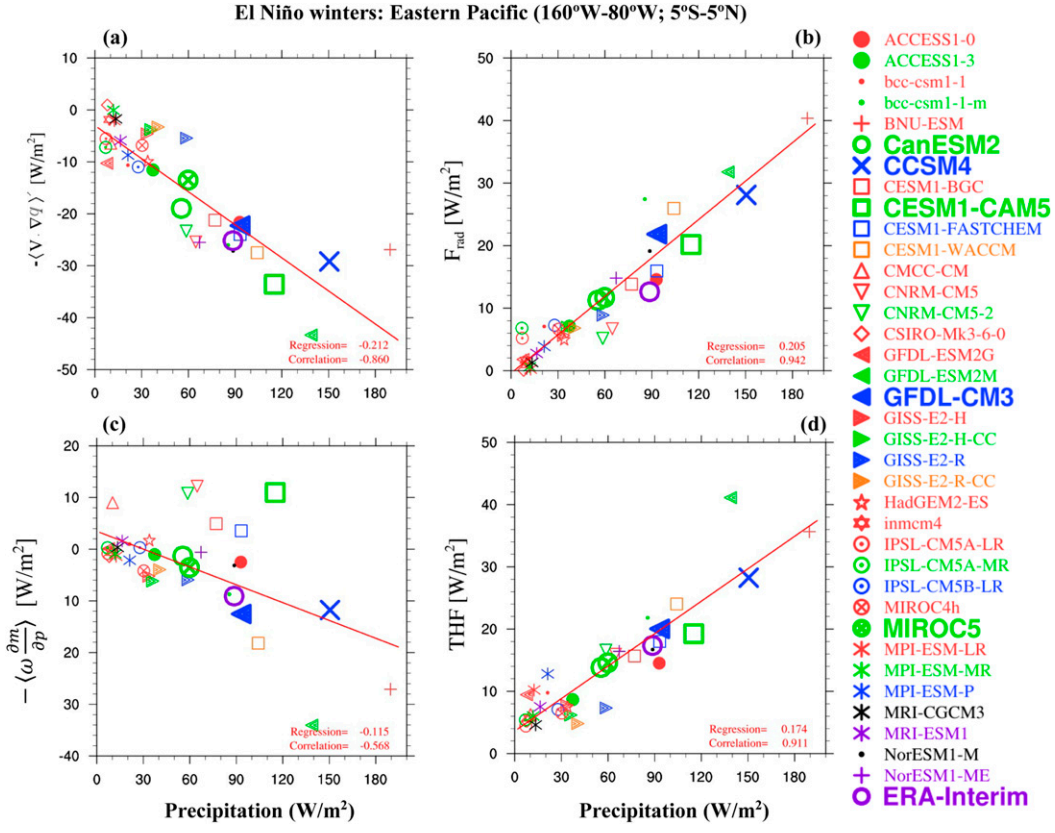


FIG. 9. As in Fig. 8, but for eastern equatorial Pacific (5°S–5°N, 160°–80°W).

precipitation anomalies, but they are not independent of each other.

### *(ii) Equatorial eastern Pacific*

ERA-I (Fig. 9) suggests that THF ($\sim$16 W m$^{-2}$) contributions to source are higher than $F_{\rm rad}$ ($\sim$11 W m$^{-2}$) while $-\langle \mathbf{V}\cdot\nabla q\rangle'$ is a stronger ($\sim -$24 W m$^{-2}$) sink compared to $-\langle \omega m_p\rangle'$ ($\sim -$10 W m$^{-2}$). Primarily due to higher observed warm SST anomalies ($\sim$1.6°C; Fig. 7a), the dominance of THF to source is consistent with earlier studies (Su and Neelin 2002; Annamalai et al. 2014). In spite of SST biases influencing the linkages (Figs. 9a–d), barring $-\langle \omega m_p\rangle'$, models represent the sign of sources (THF and $F_{\rm rad}$) and sink ($-\langle \mathbf{V}\cdot\nabla q'\rangle$) correctly. The dominant balance is between THF and $-\langle \mathbf{V}\cdot\nabla q\rangle'$. Again, the diverse response in $F_{\rm rad}$ and $-\omega m_p'$ is prevalent around precipitation values of $\sim$60–90 W m$^{-2}$, features noted in FT$_q'$ anomalies (Fig. 4f). Similar diversity is weak in THF or $-\langle \mathbf{V}\cdot\nabla q\rangle'$. With regard to $-\langle \omega m_p\rangle'$, notable scattering of model values around the regression line is noticeable with NCAR-based models capturing the "sign" of the anomalies incorrectly. As expected, there is a close link between $-\langle \omega m_p\rangle'$ and the representation of $\omega$ profiles (Fig. 10, right panels). For example, precipitation anomalies in CESM1-CAM5 are $\sim$110 W m$^{-2}$ but the intensity of the $\omega$ profile is too weak with little variation in the vertical (Fig. 10, right-middle panel). In contrast, unrealistic precipitation and the associated strong and top-heavy $\omega$ profile in GFDL-ESM2M (Fig. 10, left-middle panel) export unrealistic MSE out of the column (Fig. 9c).

### *(iii) In both regions, characteristics of $-\langle \omega m_p\rangle'$ show commonalities*

Compared to reanalysis, models that simulate weak to very weak precipitation anomalies capture weaker $\omega$ profiles with little or no vertical gradients (Fig. 10). In both regions, simulated anomalous precipitation, $-\omega m_p'$, and $\omega$ profiles are realistic in GFDL CM3, a clear improvement from GFDL-ESM2M. In accounting for the spread in $-\omega m_p'$ around precipitation values $\sim$130 W m$^{-2}$ over the central Pacific (Fig. 8c), compared to GFDL CM3, the stronger MSE export in WACCM is attributed to the intensified $\omega$ profile in the mid- to upper troposphere (600–300 hPa; Fig. 10, middle panel) resulting in a stronger upper-level divergence. Many models have unrealistic levels of maximum omega in the eastern Pacific while ERA-I also

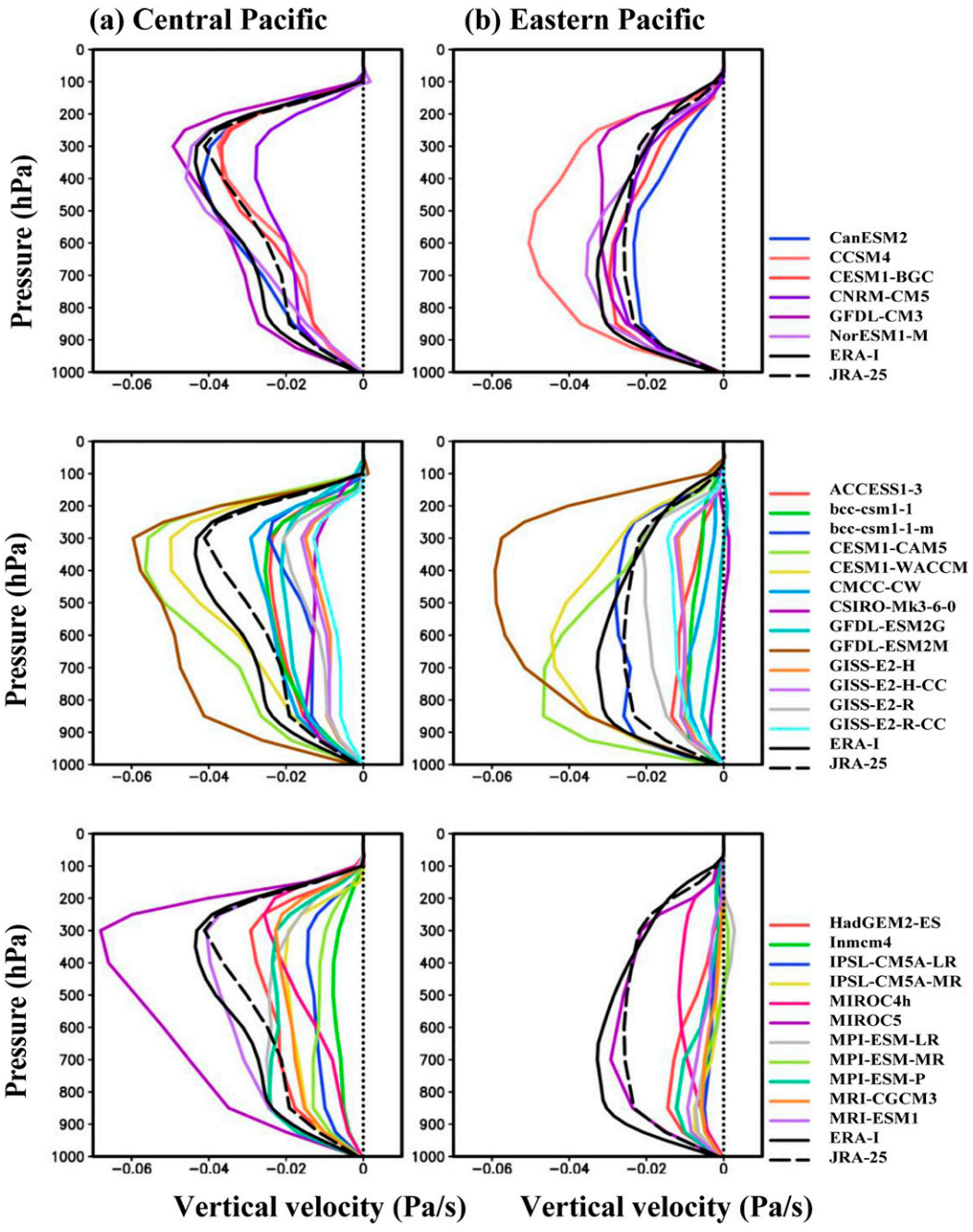


FIG. 10. CMIP5 models simulated anomalous vertical velocity (Pa $s^{-1}$) profiles averaged over the equatorial (a) central and (b) eastern Pacific. Results are for composite El Niño winters (December–February). Similar profiles constructed from ERA-I and JRA-25 are also shown. In all panels, the vertical dashed line corresponds to "zero" omega values.

depicts anomalous ascent throughout the troposphere with a maximum value of $\sim -0.025$ Pa $s^{-1}$ at around 800 hPa (i.e., bottom heavy; Fig. 10b). Over the eastern Pacific, CNRM and NCAR model versions (except CCSM4) import MSE anomalies, and MSE export in CCSM4 is only comparable to that of GFDL CM3 despite stronger precipitation anomalies in CCSM4 ($\sim$150 vs $\sim$90 W $m^{-2}$), illustrating errors in the $\omega$ profile.

### 2) La Niña

In Figs. 11 and 12, negative values in $-\langle \mathbf{V} \cdot \nabla q \rangle'$, $F_{\text{rad}}$, THF, and $-\omega m_p'$ correspond to dry advection,

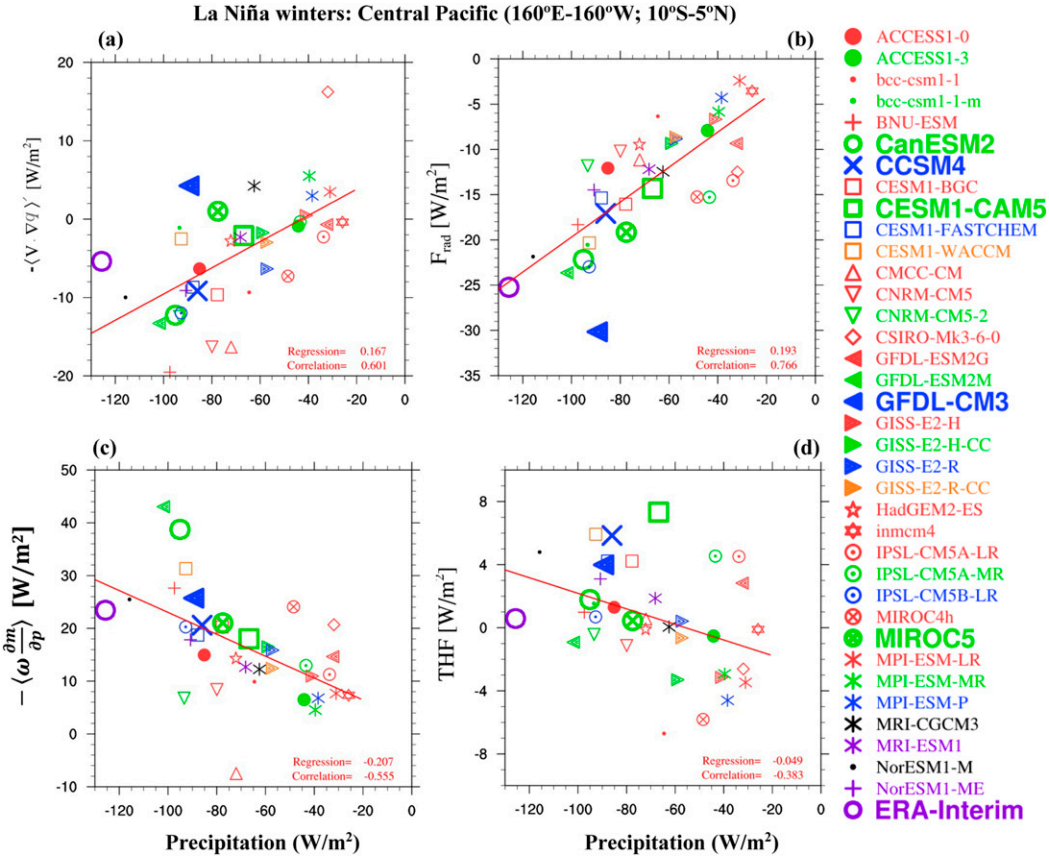


FIG. 11. As in Fig. 8, but for La Niña winters.

enhanced radiative cooling, surface fluxes from the atmosphere to ocean, and MSE import, respectively. The ERA-I results suggest that over the central Pacific, $-\omega m_p'$ is the only source, whereas $F_{\mathrm{rad}}$ and $-\langle \mathbf{V} \cdot \nabla q \rangle'$ are net sinks of column MSE, and the share from THF is near-zero. In contrast over the eastern Pacific, THF is the only sink whereas both adiabatic terms ($-\langle \mathbf{V} \cdot \nabla q \rangle'$ and $-\omega m_p'$) are net sources, and $F_{\mathrm{rad}}$ is near-zero.

*(i) Equatorial central Pacific*

The interpretation is that the low-level equatorial easterly wind anomalies east of 120°W (not shown) are effective in advecting low climatological PW air to the central Pacific (Fig. 7d), which acts as an MSE sink (Fig. 11a) and reduces convective activity. Subsequently, the increase in radiative cooling (Fig. 11b) promotes descent anomalies leading to MSE divergence at low levels (Fig. 11c). Regarding MSE sinks, all models adequately represent the sign of $F_{\mathrm{rad}}$, and $-\langle \mathbf{V} \cdot \nabla q \rangle'$ while only half of the models capture the near-zero contributions of THF and the rest capture either signs. With the exception of one model, the sign of the MSE source $-\omega m_p'$ is aptly represented. Of relevance here, diversity in all MSE terms around precipitation values from $-80$ to $-90\,\mathrm{W\,m^{-2}}$ is in agreement with similar spreads noted earlier between precipitation and CRH/FR$_q'$ anomalies (Figs. 5a,c). In La Niña winters too, constraints from model to model in representing radiation anomalies and vertical structure of vertical velocity (not shown) leading to diversity in $-\omega m_p'$ are suggested. In spite of higher cold SST anomalies in few models (e.g., MIROC5, GFDL-ESM2M, CESM1-CAM5; not shown), all models simulate less negative precipitation anomalies, possibly attributed to errors in basic state (section 5b).

*(ii) Equatorial eastern Pacific*

During La Niña winters, maximum low-level divergence occurs around 120°W (not shown). Consequently, anomalous westerlies between 120° and 80°W are effective in advecting climatological moisture from the central to eastern Pacific, acting as the dominant MSE source (Fig. 12a). All models capture the sign of $-\langle \mathbf{V} \cdot \nabla q \rangle'$ (Fig. 12a) as well as the dominant MSE sink, THF

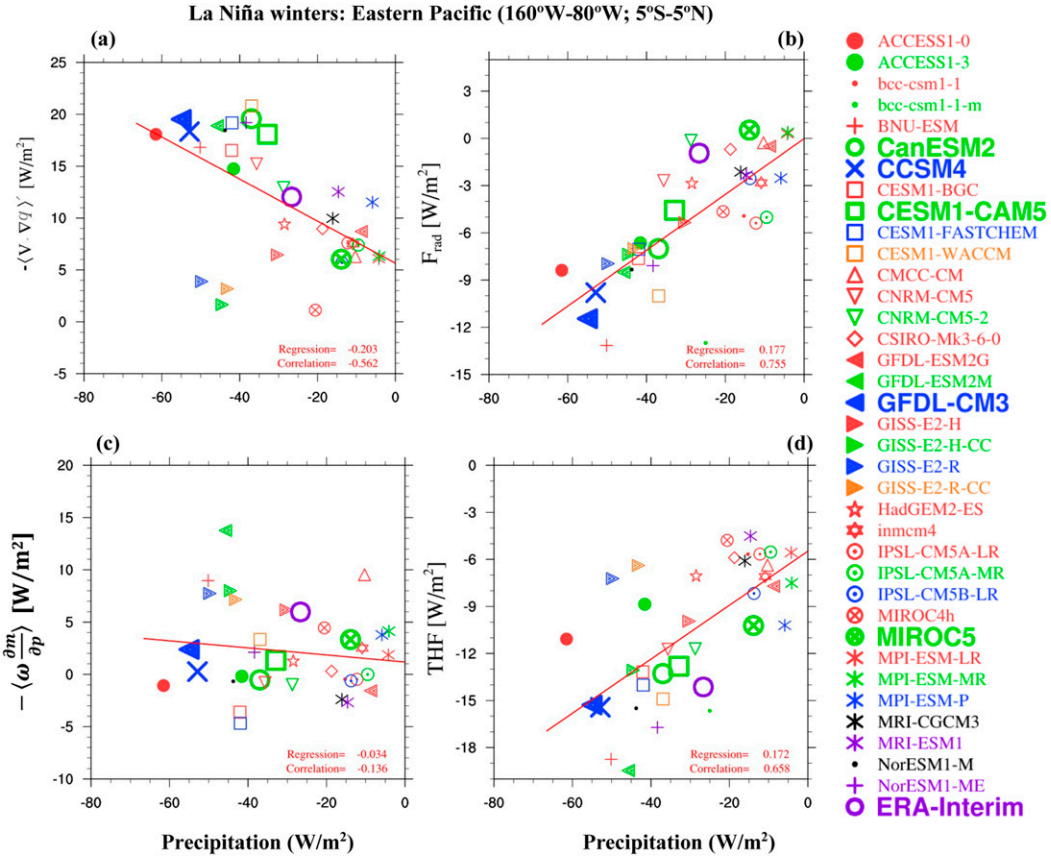


FIG. 12. As in Fig. 9, but for eastern equatorial Pacific.

(Fig. 12d). As regards $-\omega m'_p$ (Fig. 12c), an examination of $\omega$ profiles in ERA-I (not shown) shows descent throughout the troposphere with little vertical variation in the 900–600-hPa layer but decreases in the 600–300-hPa layer. In the models, either weak or bottom-heavy descent anomalies (not shown) are largely associated with near-zero $-\omega m'_p$ anomalies. Representation of $F_{\text{rad}}$ (Fig. 12b) is also problematic, implying model constrains. Here too, large spreads in all the MSE terms for precipitation anomalies from around $-40$ to $-60\,\text{W m}^{-2}$ are noticeable with similar spreads in CRH anomalies (Fig. 5).

As a final note here, NCAR-family models such as CESM1-WACCM incorporate gravity wave parameterizations in CAM4 that improve the upper atmosphere properties (e.g., Richter et al. 2010) while CESM1-BGC refers to a configuration with active biogeochemistry and a prognostic carbon cycle with nitrogen limitation (Hurrell et al. 2013; Moore et al. 2013). Comparing these two versions, ENSO-related SST and precipitation anomalies are more realistically represented in CESM1-BGC whereas they are too strong (warm/wet bias during El Niño) in CESM1-WACCM (Figs. 1a,b). Based on our diagnostics it is unclear if the realistic representation of ENSO in CESM1-BGC is due to interactive biogeochemistry impacting any particular model physics.

## 5. Discussion

Results presented in sections 3 and 4 indicate that large spreads in ENSO-related precipitation anomalies are tied to similar spreads in CRH/FT$'_q$ anomalies and to model parameterizations that determine $F_{\text{rad}}$ and $-\omega m'_p$. A careful examination indicates that large spreads in these processes are particularly strong around observed precipitation anomalies (e.g., Figs. 8b,c and 9b,c). Here, an attempt is made to understand the intrinsic physical linkages among these processes, leading us to interpret cascading errors (section 5a). Section 5b deals with models' limitations in the simulation of basic states and their plausible influence on simulated ENSO-related precipitation anomalies. Finally, results from AMIP5 diagnostics suggest that conclusions derived from

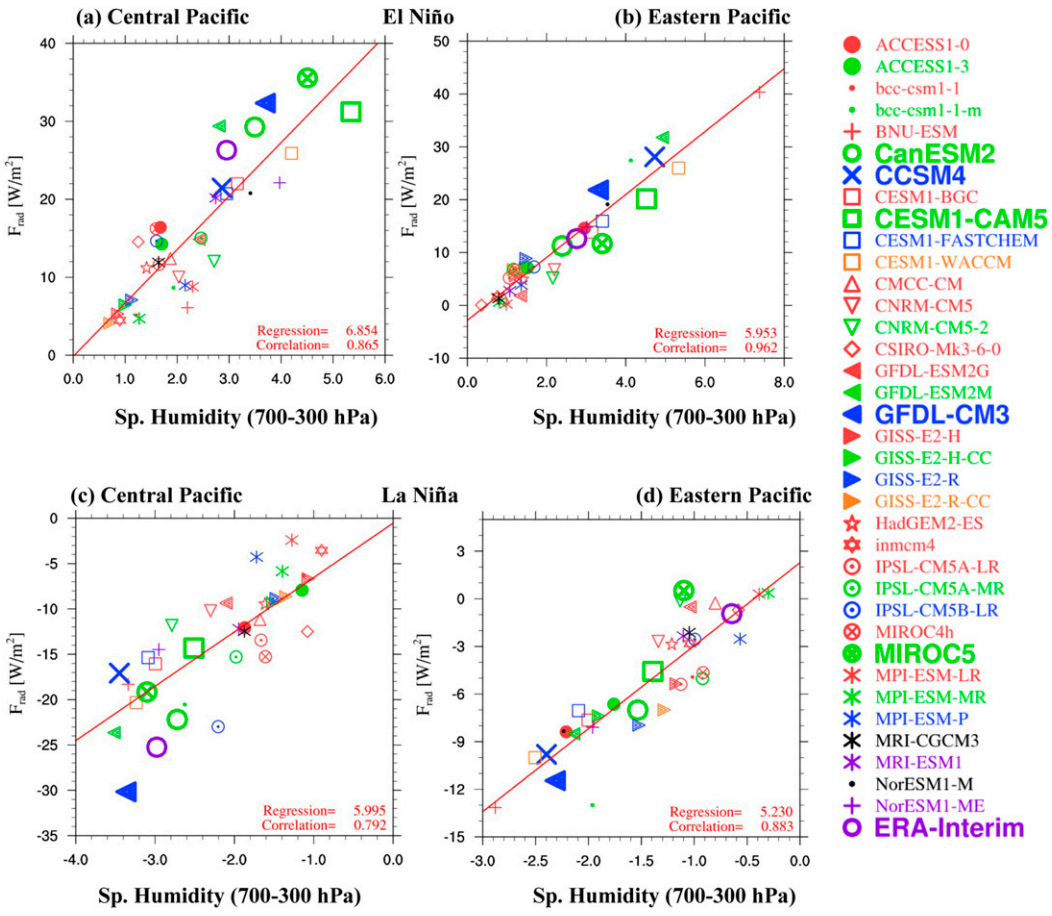


FIG. 13. (a),(b) Scatterplots between CMIP5 models simulated specific humidity in the free troposphere (700–300 hPa integrated) and net radiative flux divergence $F_{rad}$ during El Niño winters over the equatorial (a) central and (b) eastern Pacific. (c),(d) As in (a) and (b), but during La Niña winters. Results from ERA-I are also shown. In each panel, intermodel correlations and best-fit regressions are also provided.

CMIP5, particularly spreads in model processes, are not necessarily influenced by SST biases (section 5c).

### *a. Intrinsic physical linkages*

Figure 13 shows scatterplots between $FT'_q$ and $F_{rad}$ during El Niño (top) and La Niña (bottom) winters, and for the central (left) and eastern (right) Pacific regions, respectively. Similar plots between anomalous minimum or maximum vertical pressure velocity $\omega$ and $F_{rad}$ are shown in Fig. 14. During El Niño winters and in both regions, diverse responses in $F_{rad}$ to similar $FT'_q$ and $\omega$ values (top panels in Figs. 13 and 14) are particularly striking around ERA-I values. During La Niña winters too, similar diversities are noted in both regions (bottom panels in Figs. 13 and 14). The implication is that biases in representing any one of the three processes are expected to imprint on others, acknowledging the tight connection among moisture, convection, and radiation. A plausible interpretation is that $\omega$ controls vertical advection of temperature and moisture (or MSE) and therefore model biases in $\omega$ are expected to imprint in $FT'_q$ (e.g., high $FT'_q$ associated with higher convective plume buoyancy especially in the upper troposphere) with subsequent impact on high cloud occurrences with attendant biases to $F_{rad}$ (e.g., cirrus-anvil type clouds that are more effective in trapping outgoing longwave radiation). Alternatively, errors in representing cloud–convection interactions lead to net heating by clouds with a maximum at the upper troposphere, which promotes larger upper-level divergence and also lead to biases in column radiative warming with subsequent imprints on $\omega$, and finally onto $FT'_q$. Similarly, initial bias in $FT'_q$, possibly due to the insensitivity of mixing coefficients (entrainment and detrainment values) to environmental humidity, would lead to biases in $F_{rad}$ and $\omega$. As mentioned in section 1, $F_{rad}$ responds to clouds as well as feedbacks to convection through changes in omega profiles (Wolding et al. 2016; Stephens et al. 2008), $FT'_q$ is largely governed by moisture–convection interactions and $-\omega m'_p$ particularly,

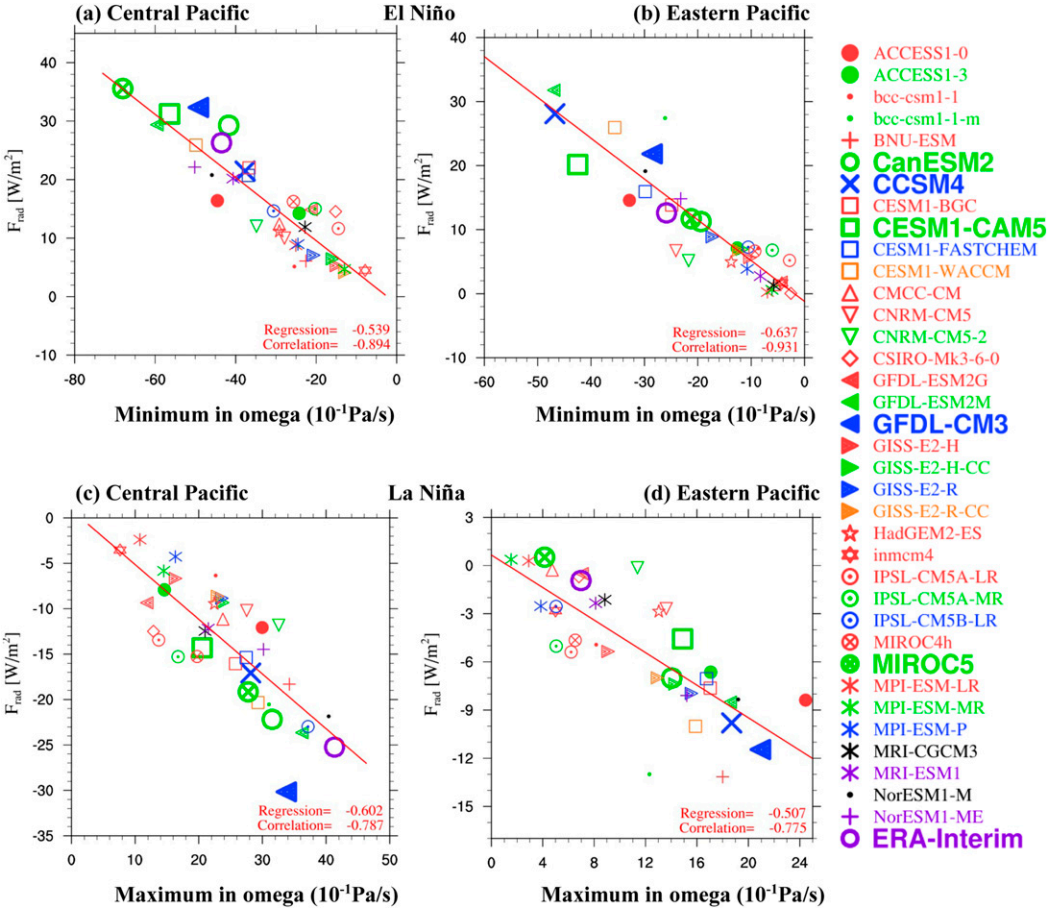


FIG. 14. (a),(b) Scatterplots between CMIP5 models simulated minimum in vertical velocity and net radiative flux divergence $F_{rad}$ during El Niño winters over the equatorial (a) central and (b) eastern Pacific. (c),(d) As in (a) and (b), but during La Niña winters. Results from ERA-I are also shown. In each panel, intermodel correlations and best-fit regressions are also provided.

and the vertical structure of $\omega$ is associated with diabatic heating profiles and cloud–convection–radiation interactions (Bretherton et al. 2006; Stephens et al. 2008; Neelin et al. 2009; Back et al. 2017). Clearly, these processes are physically linked. Irrespective of horizontal and vertical resolutions, and varied convection–cloud–radiation parameterizations in CMIP5 models, results presented in Figs. 13 and 14 suggest that accurate representations of these processes are required to advance realistic simulation of ENSO-related precipitation anomalies.

Alternatively, intermodel characteristics of MSE terms can be assessed by estimating gross moist stability (GMS), a measure of MSE export per unit convective activity (Neelin and Held 1987; Raymond et al. 2009). Climatologically, the equatorial central (eastern) Pacific experiences deep (shallow) convection accounting for a positive (negative) GMS (Yu et al. 1998; Back and Bretherton 2006). In the time mean, smaller positive values are expected to produce more rain for a given entropy forcing, permitting us to assess the GMS relationship with anomalous precipitation over the equatorial central Pacific. Following the procedures outlined in Raymond et al. (2009) and implemented in Benedict et al. (2014) and Hannah and Maloney (2014), we estimated anomalous vertical GMS (VGMS′) and effective VGMS (VGMS′$_{eff}$). Briefly, VGMS′ is given by $-\omega m_p'/-\omega q_p$, and VGMS′$_{eff}$ represents effective moist stability that includes MSE sources ($F_{rad}$ and THF) that are important for precipitation anomalies (Fig. 8), is estimated as $(-\omega m_p' + \text{Frad} + \text{THF})/-\omega q_p'$. Consistent with Raymond et al. (2009), moisture convergence $-\langle \omega m_p \rangle'$ is used as a measure of convective intensity.

The VGMS′ for ERA-I is ~0.2 (Fig. 15a); for similar values, models simulate a range of precipitation (20–170 W m$^{-2}$). As mentioned earlier (section 3b), the vertical structure of $\omega$ largely determines $-\omega m_p'$ and so VGMS′. For small negative values, models import MSE (e.g., MPI-ESM-MR) and, conversely, for high positive values models export

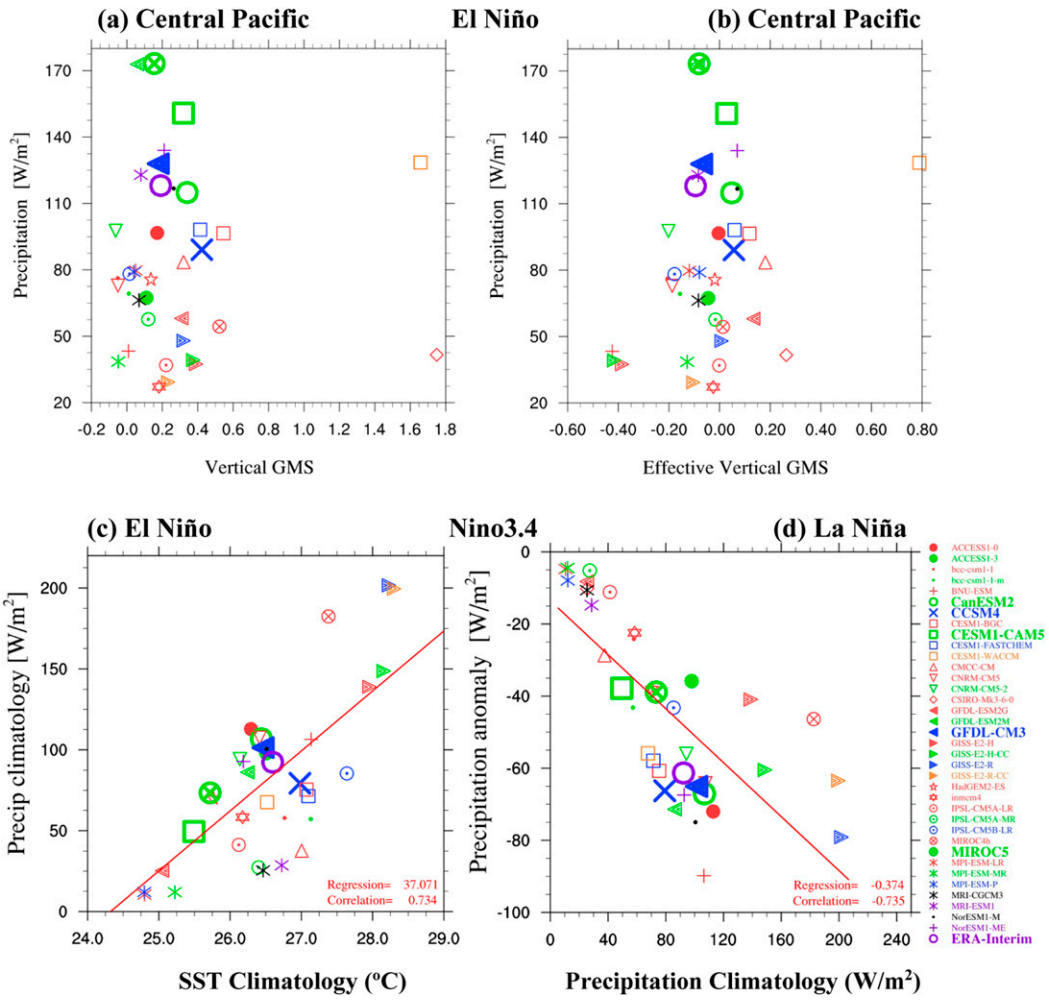


FIG. 15. (a) Scatterplots between CMIP5 models simulated anomalous vertical gross moist stability (VGMS) and precipitation. (b) As in (a), but between effective VGMS and precipitation. (c) SST climatology and precipitation climatology over the Niño-3.4 region (5°S–5°N, 120°–170°W). (d) As in (c), but for model simulated precipitation climatology and precipitation anomalies during La Niña winters over the Niño-3.4 region.

excess MSE per unit precipitation (e.g., CanESM2; Fig. 8c). The $\text{VGMS}'_{\text{eff}}$ is weakly negative for ERA-I, $\sim -0.1$ (Fig. 15b), implying the combined effect of vertical advection and MSE sources in contributing a net positive feedback on the column MSE anomalies (cf. Hannah and Maloney 2014). While many models represent weak negative $\text{VGMS}'_{\text{eff}}$, the spread in precipitation response suggests diversity in net positive feedbacks that is partly related to model compensating errors. For example, while precipitation and $\text{VGMS}'_{\text{eff}}$ are realistic in GFDL CM3, $F_{\text{rad}}$ compensates for THF. Furthermore, both MIROC5 and GFDL-ESM2M show similar $\text{VGMS}'_{\text{eff}}$ and precipitation, but compensating errors are very different in them (Fig. 8). In models that depict weak positive $\text{VGMS}'_{\text{eff}}$, vertical advection (Fig. 8c; NCAR-based models) dominates over MSE sources (Figs. 8b,d), promoting net negative feedbacks on column MSE anomalies (Fig. 4a). Thus, models that show large positive VGMS′ or weak positive $\text{VGMS}'_{\text{eff}}$, require higher entropy forcing to maintain column MSE anomalies. In climate models, for a comprehensive understanding of GMS and its role on ENSO-related precipitation anomalies, detailed diagnostics of models' climatological GMS, its spatial variation, and seasonality are required, and such analyses are currently being performed on CMIP6/AMIP6 solutions and the results will be reported elsewhere.

### b. *Basic state characteristics in CMIP5 models*

As with ENSO-related precipitation anomalies (Figs. 1a,b), spreads in the sensitivities of climatological precipitation to SST climatology during El Niño (Fig. 15c) and precipitation anomalies to climatological precipitation during La Niña (Fig. 15d) are particularly pronounced around "observed values." Comparing Figs. 15c and 1a

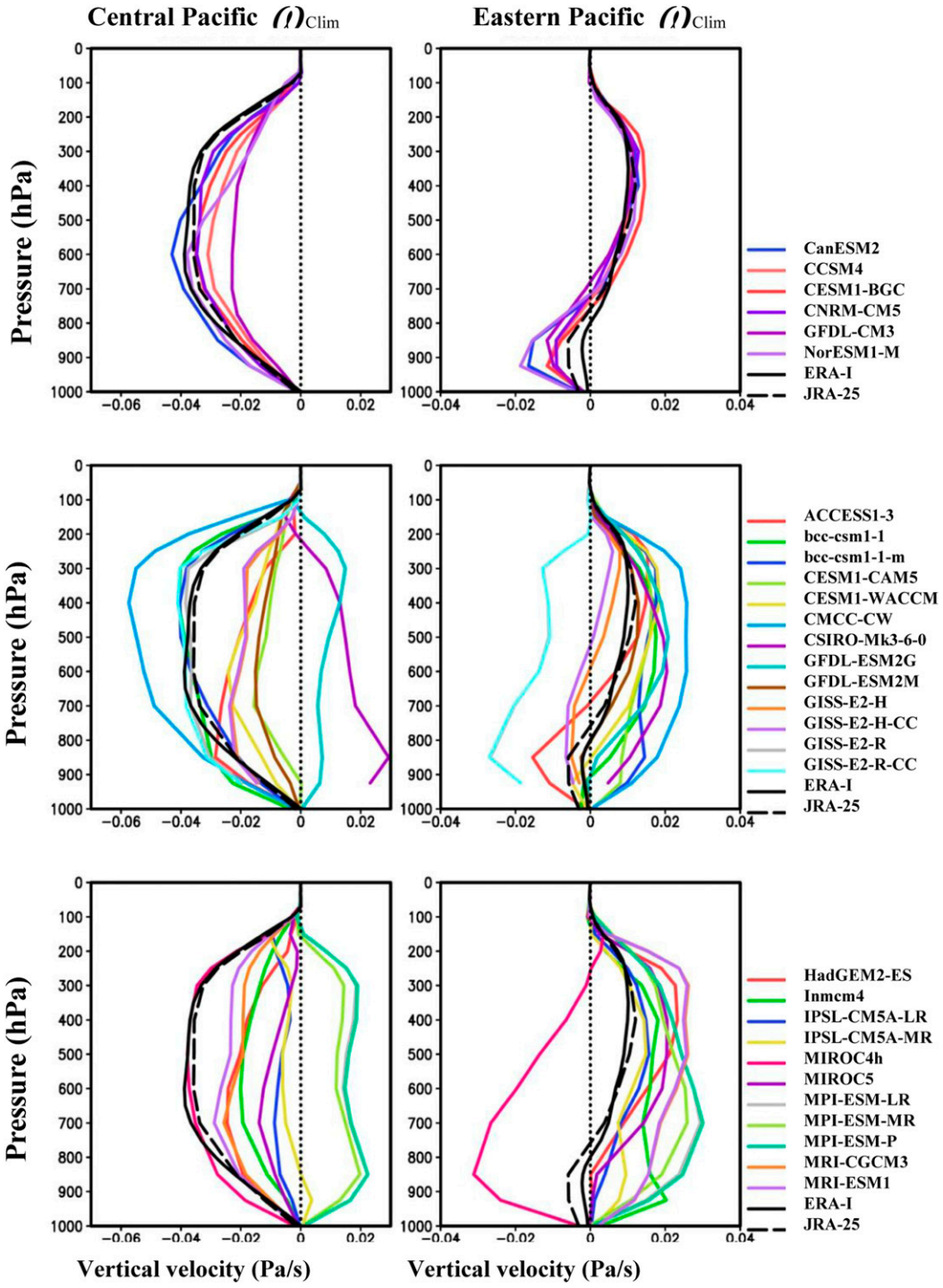


FIG. 16. CMIP5 models simulated climatological vertical velocity (Pa $s^{-1}$) profiles averaged over the equatorial (left) central and (right) eastern Pacific. Results are boreal winter season (December–February). Similar profiles constructed from ERA-I and JRA-25 are also shown. In all panels, vertical dashed line corresponds to zero omega values.

suggests that models with weak basic states in SST and precipitation such as CESM1-CAM5 and MIROC5 simulate too strong SST anomalies of ~3.0°C during El Niño but their precipitation anomalies are close to ERA-I. In sharp contrast, GISS family models capture unrealistically too strong basic states (Fig. 15c) while El Niño–related SST (~0.75°C) and precipitation (~40–50 W $m^{-2}$) anomalies are too weak (Fig. 1a). Figure 15d suggests that realistic

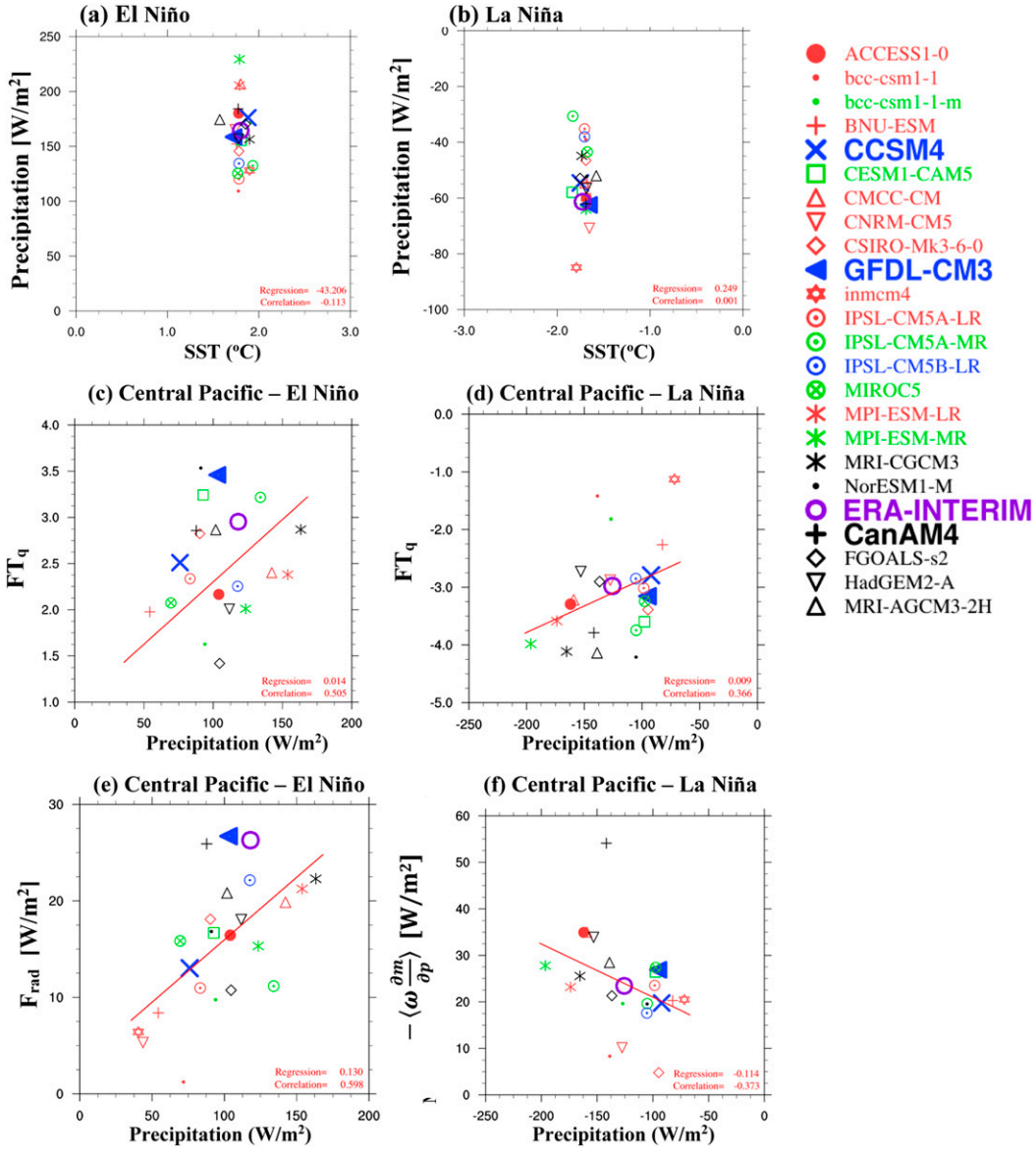


FIG. 17. Summary of diagnostics from AMIP5 solutions. (a),(b) SST and precipitation anomalies over the Niño-3.4 region for El Niño and La Niña, respectively. (c),(d) Precipitation anomalies vs anomalous $FT_q'$ over the equatorial central Pacific for El Niño and La Niña, respectively. (e) Precipitation anomalies vs $F_{rad}$ anomalies over the equatorial central Pacific for El Niño. (f) Precipitation anomalies vs vertical advection of MSE over the equatorial central Pacific for La Niña winters. The AMIP5 models' name legend is similar to CMIP5 for easy comparison. Only the last four models do not have corresponding CMIP simulations.

representation of precipitation climatology over the Niño-3.4 region (~90 W m$^{-2}$) appears to be an important metric for capturing La Niña–related precipitation anomalies (cf. Fig. 1b). During La Niña, in spite of SST anomalies close to ERA-I, CESM1-CAM5 and MIROC5 simulate weaker precipitation anomalies (Fig. 1b). In contrast, for weak SST anomalies GISS models' precipitation response is very strong. Few models that have realistic representation of basic states (e.g., GFDL CM3, NorESM1-ME, CanESM2) capture realistic ENSO-related precipitation anomalies but compensating errors exist in accounting for MSE processes.

To discern how the models perform in representing different convective regimes along the equatorial Pacific Fig. 16 shows boreal winter climatological $\omega$ profiles averaged over the central (left) and eastern (right) equatorial Pacific. In both reanalysis, consistent with Back and Bretherton (2006; their Fig. 1), there is deep circulation with a broad maximum through the midtroposphere

illustrating deep convection prevalence over the equatorial central Pacific, and bottom-heavy or shallow circulation associated with shallow convection over the eastern Pacific. Consistent with precipitation climatology (Fig. 15c), models with realistic $\omega$ profiles in both regions (Fig. 16, top panels) simulate SST and precipitation anomalies over the Niño-3.4 region reasonably well (Figs. 1a,b). Few models that have very weak climatological ascent over the central Pacific and/or missing shallow circulation over the eastern Pacific (MIROC5, CESM1-CAM5) require strong SST anomalies during El Niño to capture "realistic" precipitation anomalies (Fig. 1a). In contrast, for realistic SST in MPI-ESM-LR, precipitation anomalies are near-zero (Figs. 1a,b), attributable to modeled climatological deep descent (Fig. 16; bottom panels) associated with weak SST and precipitation climatology (Fig. 15c).

In CMIP5 models, intermodel differences in $\omega$ characteristics such as the level of maximum ascent/descent, single/double peaks, vertical gradient, and transition levels are apparent. Most models neither capture the intensity of ascent in the midlayer (700–400 hPa) over the central Pacific nor represent the shallow circulation in the bottom layer (1000–800 hPa) over the eastern Pacific. In contrast, top-heavy or bottom-heavy descent or maximum descent at both levels over the central Pacific, and ascent or descent throughout the troposphere over the eastern Pacific, are noticeable. Finally, some models (e.g., ACCESS1.3) depict bottom-heavy profiles in both regions. In climate models, the vertical structure of $\omega$ depends on the convective parameterizations employed since in the deep tropics, $\omega = Q(\partial s/\partial p)^{-1}$. Assuming little change to dry static stability ($\partial s/\partial p$), convection determines the vertical structure and intensity of $Q$ (Sobel 2007). Over the equatorial central Pacific, models' inability to represent vertical structure of $\omega$ illustrates limitations in convection to deepen. Over the equatorial eastern Pacific, models may have limitations in representing the meridional SST gradients–induced low-level convergence that determines bottom-heavy circulation. To summarize, one can conclude that CMIP5 models have constraints in representing different convective regimes and associated small-scale processes along the equatorial Pacific, and so limitations in representing climatological GMS are expected.

### c. *Results from AMIP5 diagnostics*

As mentioned earlier, SST biases in CMIP5 models are expected to influence the "association or linkages" between variables (Figs. 1a,b; section 4). To attribute precipitation spreads to model processes, we diagnosed 18 AMIP5 solutions in which the atmospheric model components employed in CMIP5 are forced with observed SST, and 4 more solutions that did not have a CMIP5 counterpart. Due to space constraints, key results from AMIP5 diagnostics that are relevant are shown in Fig. 17, and the symbols and model names for those that participated in CMIP5 are retained for easier comparison between the coupled and uncoupled solutions. Over the Niño-3.4 region during both ENSO winters, precipitation responses to prescribed "identical" SST anomalies are diverse, ranging from 100 to 240 W m$^{-2}$ during El Niño (Fig. 17a) and from −30 to −90 W m$^{-2}$ during La Niña (Fig. 17b). It is safe to mention here that spreads in modeled precipitation are due to limitations in basic states and/or model processes (e.g., $F_{\text{rad}}$, $\text{FT}'_q$).

Over the equatorial central Pacific during El Niño, $\text{FT}'_q$ (Fig. 17c) and $F_{\text{rad}}$ (Fig. 17e) depict clear spreads around observed (ERA-I) precipitation values (~110–120 W m$^{-2}$). Similarly during La Niña winters, spreads in $\text{FT}'_q$ (Fig. 17d) and $-\omega m'_p$ (Fig. 17f) in the vicinity of ERA-I precipitation values (from ~−110 to −100 W m$^{-2}$) are evident. We noted earlier (section 5a) that these processes ($F_{\text{rad}}$, $\text{FT}'_q$, and $-\omega m'_p$) are physically linked and biases in representing any one of the three processes are expected to imprint on others, acknowledging the tight connection among moisture, convection, and radiation. In summary, supporting CMIP5 results, the diverse precipitation response in AMIP5 solutions can be attributed to models' physical processes and their interactions.

## 6. Conclusions

Recognizing that equatorial Pacific precipitation anomalies are fundamental to global teleconnections during ENSO winters, the present research applies process-based diagnostics to historical simulations of CMIP5 models to identify the representation of leading processes that are important in translating ENSO-related SST anomalies into precipitation anomalies. To assess the influence of SST biases on CMIP5 diagnostics, analysis is also carried out in AMIP5 solutions. Our study addresses the following questions: 1) Do models capture the differing processes that account for regional precipitation anomalies along the equatorial Pacific? 2) Are there few leading processes that account for diversified precipitation response to similar SST forcing and vice versa?

During both El Niño and La Niña winters and in both the equatorial central and eastern Pacific regions, CMIP5 models' precipitation diversities around the observed values are tied to similar spreads in $\text{CRH}/\text{FT}'_q$ (Figs. 4–6), results duly supported by AMIP5 diagnostics (Figs. 17c,d). These results led us to hypothesize that models' ability to represent precipitation anomalies requires their ability to represent processes that determine column MSE anomalies.

For composite ENSO winters, we applied vertically integrated MSE budget and binned the terms against precipitation for the central (Figs. 8 and 10) and eastern (Figs. 9 and 11) Pacific. Examining the contributions of

MSE sources and sinks to precipitation anomalies, key results are that 1) in both winters and in both regions, models have limitations in representing the "sign" of the sources and sinks and in few models, even if they do, compensating errors dominate the budget; and 2) a diverse response in precipitation depends on model parameterizations that determine $F_{\text{rad}}$, $\text{FT}'_q$, and $-\omega m'_p$, although these processes are not independent (Figs. 8, 9, and 11–14). The implication is that biases in representing any one of the three processes are expected to imprint on others, and acknowledges the tight connection among moisture, convection, and radiation. CMIP5 results are duly supported by AMIP5 solutions (Fig. 17). Our diagnostics further show that CMIP5 models have limitations in representing basic states in SST and precipitation over the Niño-3.4 region, and in representing the different convective regimes over the central and eastern Pacific regions (Figs. 15 and 16). Few models that have realistic basic states capture ENSO-related precipitation anomalies realistically, but an examination of MSE sources and sinks shows model compensating errors (Figs. 8 and 9).

Budget diagnostics such as presented here do not necessarily close (e.g., Peters et al. 2008). Nevertheless, leading processes identified are expected to be robust (e.g., Su and Neelin 2002; Maloney 2009; Annamalai et al. 2014). Application of POD to climate simulations has its own limitations. First of all, feedbacks between diabatic and adiabatic terms are inherent and obviously limit in the identification of the initial source of model errors. Second, models' climate state results from compensating errors due to various nonlinear processes and feedbacks. To assess these issues, our ongoing work is focused on diagnosing short runs, and understanding vertical processes and cloud–convection–radiation interactions.

*Acknowledgments.* H. Annamalai acknowledges the support from NOAA-MAPP Award NA15OAR4310092 for developing process-oriented diagnostics. Dr. Hafner is thanked for his assistance in the diagnostics. Dr. Widlansky is acknowledged for his thorough editorial comments. Detailed comments and suggestions from three anonymous reviewers helped improve the manuscript. We acknowledge the World Climate Research Programme's Working Group on Coupled Modeling, which is responsible for CMIP, and we thank the climate modeling groups (listed in Table 1 of this paper) for producing and making available their model output.

## REFERENCES

Annamalai, H., J. Hafner, A. Kumar, and H. Wang, 2014: A framework for dynamical seasonal prediction of precipitation over Pacific islands. *J. Climate*, **27**, 3272–3297, https://doi.org/10.1175/JCLI-D-13-00379.1.

Back, L. E., and C. S. Bretherton, 2006: Geographic variability in the export of moist static energy and vertical motion profiles in the tropical Pacific. *Geophys. Res. Lett.*, **33**, L17810, https://doi.org/10.1029/2006GL026672.

——, Z. Hansen, and Z. Handlos, 2017: Estimating vertical motion profile top-heaviness: Reanalysis compared to satellite-based observations and stratiform rain fraction. *J. Atmos. Sci.*, **74**, 855–864, https://doi.org/10.1175/JAS-D-16-0062.1.

Bellenger, H., E. Guilyardi, J. Leloup, M. Lengaigne, and J. Vialard, 2014: ENSO representation in climate models: From CMIP3 to CMIP5. *Climate Dyn.*, **42**, 1999–2018, https://doi.org/10.1007/s00382-013-1783-z.

Benedict, J. J., E. D. Maloney, A. H. Sobel, and D. M. Frierson, 2014: Gross moist stability and MJO simulation skill in three full-physics GCMs. *J. Atmos. Sci.*, **71**, 3327–3349, https://doi.org/10.1175/JAS-D-13-0240.1.

Bony, S., J.-L. Dufresne, H. Le Treut, J.-J. Morcrette, and E. C. Senior, 2004: On dynamic and thermodynamic components of cloud changes. *Climate Dyn.*, **22**, 71–86, https://doi.org/10.1007/s00382-003-0369-6.

Bretherton, C. S., and A. Sobel, 2003: The Gill model and the weak temperature gradient approximation. *J. Atmos. Sci.*, **60**, 451–460, https://doi.org/10.1175/1520-0469(2003)060<0451:TGMATW>2.0.CO;2.

——, M. E. Peters, and L. E. Back, 2004: Relationships between water vapor path and precipitation over the tropical oceans. *J. Climate*, **17**, 1517–1528, https://doi.org/10.1175/1520-0442(2004)017<1517:RBWVPA>2.0.CO;2.

——, P. N. Blossey, and M. E. Peters, 2006: Interpretation of simple and cloud-resolving simulations of moist convection–radiation interaction with a mock-Walker circulation. *Theor. Comput. Fluid Dyn.*, **20**, 421–442, https://doi.org/10.1007/s00162-006-0029-7.

Capotondi, A., and Coauthors, 2015: Understanding ENSO diversity. *Bull. Amer. Meteor. Soc.*, **96**, 921–938, https://doi.org/10.1175/BAMS-D-13-00117.1.

Charney, J. G., 1963: A note on large-scale motions in the tropics. *J. Atmos. Sci.*, **20**, 607–609, https://doi.org/10.1175/1520-0469(1963)020<0607:ANOLSM>2.0.CO;2.

Dee, D. P., and Coauthors, 2011: The ERA-Interim reanalysis: Configuration and performance of the data assimilation system. *Quart. J. Roy. Meteor. Soc.*, **137**, 553–597, https://doi.org/10.1002/qj.828.

Derbyshire, S. H., I. Beau, P. Bechtold, J.-Y. Grandpeix, J.-M. Piriou, J.-L. Redelsperger, and P. M. M. Soares, 2004: Sensitivity of moist convection to environmental humidity. *Quart. J. Roy. Meteor. Soc.*, **130**, 3055–3079, https://doi.org/10.1256/qj.03.130.

Grabowski, W. W., 2003: MJO-like coherent structures: Sensitivity simulations using the cloud-resolving convection parameterization (CRCP). *J. Atmos. Sci.*, **60**, 847–864, https://doi.org/10.1175/1520-0469(2003)060<0847:MLCSSS>2.0.CO;2.

Graham, N. E., and T. P. Barnett, 1987: Sea surface temperature, surface wind divergence, and convection over the tropical oceans. *Science*, **238**, 657–659, https://doi.org/10.1126/science.238.4827.657.

Hannah, W., and E. D. Maloney, 2014: The moist static energy budget in NCAR CAM5 hindcasts during DYNAMO. *J. Adv. Model. Earth Syst.*, **6**, 420–440, https://doi.org/10.1002/2013MS000272.

Hartmann, D. L., L. A. Moy, and Q. Fu, 2001: Tropical convection and the energy balance at the top of the atmosphere. *J. Climate*, **14**, 4495–4511, https://doi.org/10.1175/1520-0442(2001)014<4495:TCATEB>2.0.CO;2.

Holloway, C. E., and J. D. Neelin, 2009: Moisture vertical structure, column water vapor, and tropical deep convection. *J. Atmos. Sci.*, **66**, 1665–1683, https://doi.org/10.1175/2008JAS2806.1.

Horel, J., and J. M. Wallace, 1981: Planetary-scale atmospheric phenomena associated with the Southern Oscillation. *Mon. Wea. Rev.*, **109**, 813–829, https://doi.org/10.1175/1520-0493(1981)109<0813:PSAPAW>2.0.CO;2.

Hoskins, B. J., and D. Karoly, 1981: The steady linear response of a spherical atmosphere to thermal and orographic forcing. *J. Atmos. Sci.*, **38**, 1179–1196, https://doi.org/10.1175/1520-0469(1981)038<1179:TSLROA>2.0.CO;2.

Huang, B., and Coauthors, 2015: Extended Reconstructed Sea Surface Temperature version 4 (ERSST.v4). Part I: Upgrades and intercomparisons. *J. Climate*, **28**, 911–930, https://doi.org/10.1175/JCLI-D-14-00006.1.

Huffman, G. J., and Coauthors, 2007: The TRMM Multisatellite Precipitation Analysis (TMPA): Quasi-global, multiyear, combined-sensor precipitation estimates at fine scales. *J. Hydrometeor.*, **8**, 38–55, https://doi.org/10.1175/JHM560.1.

——, R. F. Adler, D. T. Bolvin, and G. Gu, 2009: Improving the global precipitation record: GPCP version 2.1. *Geophys. Res. Lett.*, **36**, L17808, https://doi.org/10.1029/2009GL040000.

Hurrell, J. W., and Coauthors, 2013: The Community Earth System Model: A framework for collaborative research. *Bull. Amer. Meteor. Soc.*, **94**, 1339–1360, https://doi.org/10.1175/BAMS-D-12-00121.1.

Kanemaru, K., and H. Masunaga, 2013: A satellite study of the relationship between sea surface temperature and column water vapor over tropical and subtropical oceans. *J. Climate*, **26**, 4204–4218, https://doi.org/10.1175/JCLI-D-12-00307.1.

Kuang, Z., and C. S. Bretherton, 2006: A mass-flux scheme view of a high-resolution simulation of a transition from shallow to deep cumulus convection. *J. Atmos. Sci.*, **63**, 1895–1909, https://doi.org/10.1175/JAS3723.1.

Kug, J.-S., Y.-G. Ham, J.-Y. Lee, and F.-F. Jin, 2012: Improved simulation of two types of El Niño in CMIP5 models. *Environ. Res. Lett.*, **7**, 039502, https://doi.org/10.1088/1748-9326/7/3/034002.

Maloney, E. D., 2009: The moist static energy budget of a composite tropical intraseasonal oscillation in a climate model. *J. Climate*, **22**, 711–729, https://doi.org/10.1175/2008JCLI2542.1.

——, and Coauthors, 2019: Process-oriented evaluation of climate and weather forecasting models. *Bull. Amer. Meteor. Soc.*, **100**, 1665–1686, https://doi.org/10.1175/BAMS-D-18-0042.1.

Mohan, T. S., H. Annamalai, L. Marx, B. Huang, and J. Kinter, 2018: Representation of ocean–atmosphere processes associated with extended monsoon episodes over South Asia in CFSv2. *Front. Earth Sci.*, **6**, doi:10.3389/feart.2018.00009.

Moore, J. K., K. Lindsay, S. C. Doney, M. C. Long, and K. Misumi, 2013: Marine ecosystem dynamics and biogeochemical cycling in the Community Earth System model [CESM1(BGC)]: Comparison of the 1990s with the 2090s under the RCP4.5 and RCP8.5 scenarios. *J. Climate*, **26**, 9291–9312, https://doi.org/10.1175/JCLI-D-12-00566.1.

Nagura, M., J. P. McCreary, and H. Annamalai, 2018: Origins of coupled model biases in the Arabian Sea climatological state. *J. Climate*, **31**, 2005–2029, https://doi.org/10.1175/JCLI-D-17-0417.1.

Neelin, J. D., and I. M. Held, 1987: Modeling tropical convergence based on the moist static energy budget. *Mon. Wea. Rev.*, **115**, 3–12, https://doi.org/10.1175/1520-0493(1987)115<0003:MTCBOT>2.0.CO;2.

——, O. Peters, and K. Hales, 2009: The transition to strong convection. *J. Atmos. Sci.*, **66**, 2367–2384, https://doi.org/10.1175/2009JAS2962.1.

Numaguti, A., R. Oki, K. Nakamura, K. Tsuboki, N. Misawa, T. Aisai, and Y.-M. Kodama, 1995: 4–5-day-period variation and low-level dry air observed in the equatorial western Pacific during the TOGA-COARE IOP. *J. Meteor. Soc. Japan*, **73**, 267–290, https://doi.org/10.2151/jmsj1965.73.2B_267.

Onogi, K. J., and Coauthors, 2007: The JRA-25 reanalysis. *J. Meteor. Soc. Japan*, **85**, 369–432, https://doi.org/10.2151/jmsj.85.369.

Peters, M. E., Z. Kuang, and C. C. Walker, 2008: Analysis of atmospheric energy transport in ERA-40 and implications for simple models of the mean tropical circulation. *J. Climate*, **21**, 5229–5241, https://doi.org/10.1175/2008JCLI2073.1.

Phillips, T. J., and Coauthors, 2004: Evaluation parameterizations in general circulation models: Climate simulation meets weather prediction. *Bull. Amer. Meteor. Soc.*, **85**, 1903–1916, https://doi.org/10.1175/BAMS-85-12-1903.

Raymond, D. J., 1995: Regulation of moist convection over the west Pacific warm pool. *J. Atmos. Sci.*, **52**, 3945–3959, https://doi.org/10.1175/1520-0469(1995)052<3945:ROMCOT>2.0.CO;2.

——, 2000: Thermodynamic control of tropical rainfall. *Quart. J. Roy. Meteor. Soc.*, **126**, 889–898, https://doi.org/10.1002/qj.49712656406.

——, S. L. Sessions, A. H. Sobel, and Z. Fuchs, 2009: The mechanics of gross moist stability. *J. Adv. Model. Earth Syst.*, **1**, 1–20, https://doi.org/10.3894/JAMES.2009.1.9.

Rayner, N. A., D. E. Parker, E. B. Horton, C. K. Folland, L. V. Alexander, D. P. Rowell, E. C. Kent, and A. Kaplan, 2003: Global analyses of sea surface temperature, sea ice, and night marine air temperature since the late nineteenth century. *J. Geophys. Res.*, **108**, 4407, https://doi.org/10.1029/2002JD002670.

Richter, J. H., F. Sassi, and R. Garcia, 2010: Toward a physically based gravity wave source parameterization in a general circulation model. *J. Atmos. Sci.*, **67**, 136–156, https://doi.org/10.1175/2009JAS3112.1.

Rienecker, M. M., and Coauthors, 2011: MERRA—NASA's Modern-Era Retrospective Analysis for Research and Applications. *J. Climate*, **24**, 3624–3648, https://doi.org/10.1175/JCLI-D-11-00015.1.

Saha, S. S., and Coauthors, 2010: The NCEP Climate Forecast System Reanalysis. *Bull. Amer. Meteor. Soc.*, **91**, 1015–1058, https://doi.org/10.1175/2010BAMS3001.1.

Slingo, J. M., and Coauthors, 1996: Intraseasonal oscillation in 15 atmospheric general circulation models: Results from an AMIP diagnostic subproject. *Climate Dyn.*, **12**, 325–357, https://doi.org/10.1007/BF00231106.

Sobel, A. H., 2007: Simple models of ensemble-averaged tropical precipitation and surface wind, given the sea surface temperature. *The Global Circulation of the Atmosphere*, T. Schneider and A. H. Sobel Eds., Princeton University Press, 219– 251.

——, J. Nilsson, and L. M. Polvani, 2001: The weak temperature gradient approximation and balanced tropical moisture waves. *J. Atmos. Sci.*, **58**, 3650–3665, https://doi.org/10.1175/1520-0469(2001)058<3650:TWTGAA>2.0.CO;2.

Sperber, K. R., H. Annamalai, I.-S. Kang, A. Kitoh, A. Moise, A. Turner, B. Wang, and T. Zhou, 2013: The Asian summer monsoon: An intercomparison of CMIP5 vs. CMIP3 simulations of the late 20th century. *Climate Dyn.*, **41**, 2711–2744, https://doi.org/10.1007/s00382-012-1607-6.

Stephens, G., S. van den Heever, and L. Pakula, 2008: Radiative–convective feedbacks in idealized states of radiative–convective equilibrium. *J. Atmos. Sci.*, **65**, 3899–3916, https://doi.org/10.1175/2008JAS2524.1.

Su, H., and J. D. Neelin, 2002: Teleconnection mechanisms for tropical Pacific descent anomalies during El Niño. *J. Atmos. Sci.*, **59**, 2694–2712, https://doi.org/10.1175/1520-0469(2002)059<2694:TMFTPD>2.0.CO;2.

Taylor, K. E., R. J. Stouffer, and G. A. Meehl, 2012: An overview of CMIP5 and the experiment design. *Bull. Amer. Meteor. Soc.*, **93**, 485–498, https://doi.org/10.1175/BAMS-D-11-00094.1.

Trenberth, K. E., J. Fasullo, and L. Smith, 2005: Trends and variability in column-integrated atmospheric water vapor. *Climate Dyn.*, **24**, 741–758, https://doi.org/10.1007/s00382-005-0017-4.

Tulich, S., and B. E. Mapes, 2010: Transient environmental sensitivities of explicitly simulated tropical convection. *J. Atmos. Sci.*, **67**, 923–940, https://doi.org/10.1175/2009JAS3277.1.

Ushiyama, T., S. Satoh, and K. Takeuchi, 1995: Time and spatial variations of mesoscale rainfalls and their relation to the large-scale field in the western tropical Pacific. *J. Meteor. Soc. Japan*, **73**, 379–392, https://doi.org/10.2151/jmsj1965.73.2B_379.

Wentz, F. J., C. L. Genteman, D. K. Smith, and D. Chelton, 2000: Satellite measurements of sea surface temperature. *Science*, **288**, 847–850, https://doi.org/10.1126/science.288.5467.847.

Widlansky, M. J., P. J. Webster, and C. D. Hoyos, 2011: On the location and orientation of the South Pacific convergence zone. *Climate Dyn.*, **36**, 561–578, https://doi.org/10.1007/s00382-010-0871-6.

Wielicki, B. A., B. R. Barkstrom, E. F. Harrison, R. B. Lee III, G. L. Smith, and J. E. Cooper, 1996: Clouds and the Earth's Radiant Energy System (CERES): An Earth observing system experiment. *Bull. Amer. Meteor. Soc.*, **77**, 853–868, https://doi.org/10.1175/1520-0477(1996)077<0853:CATERE>2.0.CO;2.

Wolding, B. O., E. D. Maloney, and M. Branson, 2016: Vertically resolved weak temperature gradient analysis of the Madden–Julian oscillation in SP-CESM. *J. Adv. Model. Earth Syst.*, **8**, 1586–1619, https://doi.org/10.1002/2016MS000724.

Woolnough, S. J., and Coauthors, 2010: Modeling convective processes during the suppressed phase of the Madden–Julian oscillation: Comparing single-column models with cloud resolving models. *Quart. J. Roy. Meteor. Soc.*, **136**, 333–353, https://doi.org/10.1002/qj.568.

Yu, J., C. Chou, and J. D. Neelin, 1998: Estimating the gross moist stability of the tropical atmosphere. *J. Atmos. Sci.*, **55**, 1354–1372, https://doi.org/10.1175/1520-0469(1998)055<1354:ETGMSO>2.0.CO;2.

Yu, L., X. Jin, and R. A. Weller, 2008: Multidecade global flux datasets from the Objectively Analyzed Air–Sea Fluxes (OAFlux) project: Latent and sensible heat fluxes, ocean evaporation, and related surface meteorological variables. OAFlux Project Tech. Rep. OA-2008-01, 64 pp.

Yuan, L., and D. L. Hartmann, 2008: Spatial and temporal dependence of clouds and their radiative impacts on the large-scale vertical velocity profile. *J. Geophys. Res.*, **113**, D19201, https://doi.org/10.1029/2007JD009722.

Zhao, M., and Coauthors, 2018: The GFDL global atmosphere and land model AM4.0/LM4.0: 2. Model description, sensitivity studies, and tuning strategies. *J. Adv. Model. Earth Syst.*, **10**, 735–769, https://doi.org/10.1002/2017MS001209.